DESIGN OF A SPACE-BORNE AUTONOMOUS INFRARED TRACKING SYSTEM

THESIS

Matthew B. Kimsal, Captain, USAF

AFIT/GA/ENY/04-M02

DEPARTMENT OF THE AIR FORCE
AIR UNIVERSITY

AIR FORCE INSTITUTE OF TECHNOLOGY

Wright-Patterson Air Force Base, Ohio

AFIT/GA/ENY/04-M02

DESIGN OF A SPACE-BORNE AUTONOMOUS INFRARED TRACKING SYSTEM

THESIS

Presented to the Faculty

Department of Aeronautics and Astronautics

Graduate School of Engineering and Management

Air Force Institute of Technology

Air University

Air Education and Training Command

In Partial Fulfillment of the Requirements for the

Degree of Master of Science in Astronautical Engineering

Matthew B. Kimsal, BS

Captain, USAF

March 2004

AFIT/GA/ENY/04-M02

DESIGN OF A SPACE-BORNE AUTONOMOUS INFRARED TRACKING SYSTEM

Matthew B. Kimsal, BS
Captain, USAF

Approved:

// signed //

Maj Richard G. Cobb (Chairman) date

// signed //

Steven A. Tragesser (Member) date

// signed //

Maj Joerg D. Walter (Member) date

Abstract

Complete characterization of the space environment in support of the United States' goal of Space Situational Awareness is not currently achievable. When confronted with recent increases in the deployment and miniaturization of microsatellites by numerous nations, the questions of foreign space capabilities are magnified. This study sought to determine the feasibility of and experimentally demonstrate a microsatellite capability to autonomously loiter about and track a target satellite.

Various methods of passive remote sensing were investigated to determine the best means of detecting and tracking a target in space. Microbolometer-based infrared sensors were identified as the best sensor for several reasons, primarily due to their ability to track in the absence of light. A representative system was constructed for demonstration in AFIT's SIMSAT laboratory.

Software modeling results identified open-loop instability, and therefore the requirement for closed-loop control. A simple PD control algorithm served as the basis for control, and a pseudo-feed-forward term was added to improve the results. The feed-forward term was derived form orbital dynamics as the rate at which the chase satellite traverses around an ellipse formed in the target's frame of reference. Reduction in pointing errors of up to 67% were found in simulations. Non-optimal yet successful tracking results were obtained in the laboratory with a hardware-in-the-loop model for both step and moving inputs. With minor modification, this infrared tracking system could be implemented onboard a microsatellite.

For My Wife

Acknowledgments

I would first like to thank God for the blessings He has bestowed upon me throughout my life. Without His provisions, I would not be where I am today.

I must also give great credit to my advisor, Maj Rich Cobb. Without his guidance, wisdom, and timely insight, I would not be where I am today.

Lastly, I would like to thank my wife. Without her love, understanding, and support, I would not be where I am today. She has taught me more than AFIT ever could.

Matthew B. Kimsal

Table of Contents

Page

Abstract iv

Acknowledgments vi

List of Figures ix

List of Tables xi

I. Introduction 1

- Space Control 2
  - Ground-based Characterization 3
  - Space-based Characterization 3
- Current Efforts in Close-Proximity Orbiting and Rendezvous 4
- Research Objectives 6
- Thesis Outline 7

II. Background 8

- Passive Sensing 8
- Similar Efforts 9
- Methods of Detection 11
  - Electromagnetic Radiation 12
  - Infrared Radiation Characteristics 13
- Infrared Detector Selection 15
- Infrared Modeling of Target Satellite 17
- Orbital Dynamics of Close Spacecraft Formations 22

III. Experimental Setup 27

- Determination of Required Yaw Rate 27
- Determination of Image Plane Centering Algorithm 29
- Software Modeling of Test Cases 31
- The SIMSAT 33
  - New Equipment 35
  - Hardware Experimental Process 36

IV. Results 39

- Theoretical Case Results 39
  - Uncontrolled Case 39

Page

Controlled Case....42
Laboratory Results....44
$\dot{\tilde{b}}$ Commanding....44
Infrared Camera Tracking of a Heat Source....48
Tracking of a Moving Heat Source....52

V. Conclusions and Recommendations....58

Conclusions....58
Recommendations for Future Study....60

Appendix A. Calculation of Maximum Range for Detection....62

Appendix B. Calculation of SIMSAT Moments of Inertia....65

Appendix C. New Equipment Specifications....67

Appendix D. Matlab Program Code....69

Appendix E. Characterization of Yaw Gyro Drift....78

Appendix F. Simulation Model Library....80

Bibliography....85

Vita....88

List of Figures

Figure Page

1. Image of Delta II Second Stage Taken by XSS-10 5
2. The Electromagnetic Spectrum 11
3. Radiant Exitance for a Blackbody at 300K (7) 14
4. Indigo Systems' Merlin and Omega Bolometer Cameras 19
5. Intensity Map of Top-of-Atmosphere Emitted Longwave Radiation 20
6. Relative Frame of Target in Inertial Space 24
7. Chase Vehicle Motion in Target Relative Frame 26
8. Simulink Model Simulating On-Orbit Motion 32
9. Simulink Model Simulating Laboratory Conditions 33
10. SIMSAT Atop Its Air Pedestal 34
11. New Equipment Added for Experiment 35
12. Depiction of Relative Path "Slip" Throughout 10-hour LEO Orbit 40
13. Angular Difference Between Modeled and J_2–Perturbed Orbit (LEO Case) 41
14. Angular Difference Between Modeled and J_2–Perturbed Orbit (GEO Case) 41
15. $\tilde{b}$ vs. Time for GEO and LEO Cases 42
16. $\tilde{b}$ Differences vs. Time for GEO and LEO Cases 43
17. Initial Measurements of SIMSAT Body Yaw Rate with Forced $\dot{\tilde{b}}$ 45
18. SIMSAT Unforced Acceleration: Average with Trendline 46
19. SIMSAT Yaw Angle and Rate vs. Time (Positive Case) 46

Figure Page

20. SIMSAT Yaw Angle and Rate vs. Time (Negative Case) 47

21. Modeled (with Known Disturbance) and Actual Yaw Rates 48

22. Heat Source Moving Across the Image Plane over Time 49

23. Simulink Model of SIMSAT System 50

24. Closed-Loop Simulink Results for a 5º Step Input 50

25. SIMSAT Step Input Behavior 51

26. Simulink Model of SIMSAT System for Moving Heat Source 53

27. Closed-Loop Simulink Results for a Moving Heat Source 53

28. Angular Position Difference Between Heat Source and SIMSAT 54

29. Top View of Hardware Experimental Setup 55

30. Results of Tracking Test with Moving Target and Integrated $\dot{\tilde{b}}$ 56

31. Angular Error Between Target and Image Calculation for Moving Target Test 57

E-1. Yaw Gyro Drift Angles After Various Amounts of Warm-up Time 78

E-2. Average Yaw Gyro Drift and a Polynomial Approximation 79

List of Tables

Table Page

1. Image Resolution Requirements for Satellite Mission & Payload Assessment 3

2. Orbital Data Used in Theoretical Simulations 39

DESIGN OF A SPACE-BORNE AUTONOMOUS INFRARED TRACKING SYSTEM

I. Introduction

In recent years, technological advances have paved the way for reduced size of spacecraft components. Microsatellites and nanosatellites, defined as those satellites weighing less than 100 kg and 10 kg, respectively, are capable of handling many of the same tasks as their much larger counterparts from just a few years ago. The new found technical capabilities of microsatellites have furthered the interest in many speculative satellite missions, including the ideas of satellite formation flying, inspecting satellites, and servicing satellites.

Inspecting satellites are conceptualized as small satellites that linger around a primary satellite, autonomously examining it for operational flaws. Servicing satellites would carry this mission one step further: repairing or replacing a vital component of another satellite in the event of degradation. These types of satellites have become a topic of great interest, and their practicality grows stronger annually. Indeed, recent tests have shown the viability of close-proximity orbiting microsatellites with simple autonomous capabilities. Though the objectives of these designs are exploratory and non-aggressive in nature, it is entirely possible that the principles behind this technology could be used for alternative, non-cooperative means.

1.1 Space Control

With the United States' substantial dependence on its space assets, attention must be devoted to monitoring the space environment. This monitoring is frequently referred to as Space Situational Awareness (SSA), and includes knowledge of the status, location, and capabilities of not only U.S. space assets, but also those of the U.S.'s allies and adversaries (19). Sound SSA enables both offensive and defensive counterspace. Together the three compose the basic elements of Aerospace Control (6), which is one of the preeminent military doctrines of current national interest.

Defensive counterspace is the concept of protecting one's friendly assets, while offensive counterspace is the concept of negating an adversary's assets. Both are at the forefront of concern for national space policymakers; concern must be given not only to the capabilities and intentions of the United States, but also to those of any space-capable nation or organization. In his report to the Commission to Assess United States National Security Space Management and Organization, Mr. Tom Wilson addresses the threat of foreign counterspace succinctly (29).

> "The U.S. reliance on space, coupled with the growing amount of information available about our space systems, increases the likelihood that our adversaries will employ counterspace weapons technologies."

Thus counterspace and Space Situational Awareness are both topics of great import. In order to support them, characterization of the space environment and other information must either be collected from earth or by a space-borne payload itself.

1.1.1 Ground-based Characterization

Current capabilities for ground-based detection of resident space objects are inadequate. Most technology employed is antiquated (3), and provides only limited resolution for objects in low-earth orbiting (LEO) altitudes. According to Worden, microsatellite-sized objects are undetectable at geosynchronous range (30). Furthermore, space object identification (SOI) is even more difficult with current resources. Table 1 details the required resolution for satellite payload assessment in LEO (24). With no *a priori* information, the problem of non-cooperative SSA is magnified.

Table 1. Image Resolution Requirements for Satellite Mission & Payload Assessment (24)

Satellite Size	Diameter (m)	Resolution Requirement (cm)	US capability
Large	>15	>50	Current
Medium	15-5	16	Current
Small	5-2.5	8	Limit
Mini	2.5-0.6	2	Beyond

1.1.2 Space-based Characterization

Autonomous detection and identification of space objects is virtually non-existent. The current Air Force Space Surveillance Network (SSN) has only one space-borne sensor. This sensor is called the space-based visible (SBV) sensor and was launched as an additional payload aboard the Midcourse Space Experiment (MSX) satellite (3). It is reported to image objects well, though this is not its original design intent.

An Air Force developmental program known as the rapid attack, identification, detection, and reporting system (RAIDRS) seeks to combine a suite of different sensors aboard a spacecraft. It would give the ability to detect jamming, irradiation, or other

offensive activities (3). A similar yet far less sophisticated subsystem dubbed the Compact Environmental Anomaly Sensor (CEASE) has been developed by AFRL (1). A subsystem such as one of these could be the solution to space-based detection, though complete identification may still require even more information. Furthermore, widespread usage of either of these systems is not in the near future.

1.2 Current Efforts in Close-Proximity Orbiting and Rendezvous

Within the past several years, several countries have demonstrated significant accomplishments in the areas of proximity orbiting and rendezvous.

Japan launched its ETS-VII experiment in November 1997. The experiment consisted of one target and one chaser satellite. Successful demonstration of rendezvous of the two satellites was conducted from separations of both 2 m and 12 km (3). Additionally, a robotic arm attached to one of the spacecraft repeatedly performed simplistic "peg-in-hole" tests over a two year duration.

China and Great Britain have also demonstrated the ability to launch and fly in formation with microsatellites. The Chinese Tsinghua 1 satellite was developed in conjunction with the Surrey Satellite Technology, Ltd., and was launched in June 2000 alongside Britain's SNAP-1 satellite (23). Though SNAP-1 was the satellite that was reported to have successfully maneuvered around Tsinghua 1, a similar plan with the roles of each reversed seems to have been planned at one point (23).

The United States entered the arena in 2003 with the short yet highly successful mission of the XSS-10 microsatellite. Developed by the Air Force Research Laboratory's (AFRL) Space Vehicles Directorate, the 30 kg satellite autonomously

orbited its Delta II second stage within 100 m. Figure 1 is an image taken by XSS-10 of the second stage. The satellite was then commanded into a dormant stage, and later awakened to full operational capability (2). Figure 1 is an image taken by XSS-10 of the Delta II second stage that launched it. The Air Force plans to launch a follow-on experiment in the form of XSS-11, a similar microsatellite with increased payload capabilities, in late 2004.

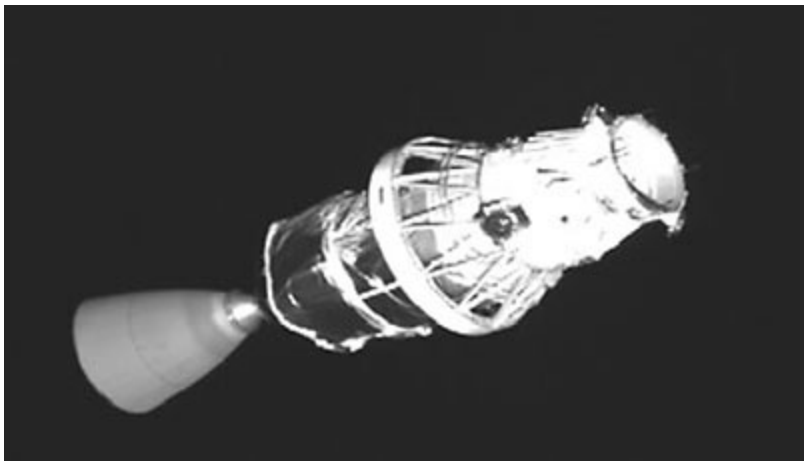

Figure 1. Image of Delta II Second Stage Taken by XSS-10 (3)

The Defense Advanced Research Projects Agency (DARPA) is currently developing an experimental two-satellite system that will be used to demonstrate the capabilities of autonomous on-orbit servicing (27). One satellite, designated the Next Genereation Serviceable Satellite (NextSat) will act as the receiver, and the other, dubbed the Autonomous Space Transport and Robotic Orbiter (ASTRO), will demonstrate rendezvous, docking, and fuel transfer techniques (27). Though not yet operational, this concept may prove to be one of the enabling technologies for space-based laser and other conceptual programs. Thus it is clearly at a high level of national interest

Many commercial satellite companies also recognize the various potential applications for microsatellites. One example is the AeroAstro company, who is in development of a microsatellite named the Escort. Accordingly, the company's brochure for the satellite mentions other applications such as "monitor space around a large satellite to detect attacks" and "stealthily attack to permanently or temporarily disable a large satellite" (10).

1.3 Research Objectives

The goal of this study is to develop a notional system that will allow surreptitious circumnavigation and tracking of one satellite about another. Such a satellite could loiter about its target until some time at which it could institute any number of potentially detrimental actions to include jamming, interception, and possibly even rendezvous (though this paper will not address this last possibility). The spirit of this study is to envision a "low-tech" approach to a satellite tracking system—one that could be employed by a rogue team with little money and expertise. This main objective is broken into three subobjectives as follows:

1. Selection of a means of detection of the target satellite
2. Determination of the orbital motion for a chase vehicle
3. Determination of a control algorithm that will allow tracking of a target.

1.4 Thesis Outline

Chapter 1 has introduced the motivation for a study involving possibility of covert circumnavigation and tracking. The determination of the feasibility of such a system is first approached with an investigation of measurement and detection systems in order to determine the most appropriate means of object detection. Next, classical orbital dynamics will be exploited in order to investigate the relative motion between the chase and target vehicles. Finally, elementary control theory will be considered and applied to both a simulation platform as well as experimental hardware.

II. Background

In order to successfully navigate about a target space object, some nominal amount of data about the target must be obtained. The acquisition of information about an object without being in direct physical contact with it is defined as remote sensing (9). The methods that are used to acquire the information about an object are generally classified as electromagnetic, acoustic, or potential (9). Each of these manners of information acquisition will be discussed. However, before these three areas are investigated, a prerequisite requirement for a passive sensor is explained, and several current efforts in the field are examined.

2.1 Passive Sensing

As stated earlier in the assumptions of this paper, the preferred method of detection is a passive one. This is due to the covert nature of the proposed mission. Radiating a satellite with radar, laser, or lidar could potentially trigger some type of status monitoring subsystem on the target satellite. The CEASE module described in Chapter I has been developed and placed in orbit by the Space Vehicles Directorate of the Air Force Research Laboratory (1). Though its intended mission is to monitor deep dielectric charging and other near-earth space environment effects on a satellite, modifications could potentially allow for the monitoring of other low-power irradiation. As mentioned in Chapter I, a similar system known as RAIDRS is also under development. RAIDRS would be able to detect "spy" satellites with a suite of various types of sensors. Then for the purposes of this study, it is assumed that satellites of interest either have, or will have,

the capability of detecting when they are being interrogated by electromagnetic radiation. Therefore only passive detection will be considered herein.

2.2 Similar Efforts

Technologies to improve rendezvous have been researched to a limited degree. Investigation of current efforts in this topic turned up several studies, but all centered around the same few principles. Junkins, et. al., introduced a method of facilitating rendezvous and docking by using a series of LED lights placed strategically on the target (15). This method is not applicable in this study as its primary assumption is that the target is a cooperative target. Other strategies to assist in the rendezvous of non-cooperative targets are mainly centered around spatial and attitude information. The field of autonomous machine vision continues to expand and has provided the foundation for many of these strategies.

Efforts to extract spatial information about an object through optical remote sensing have been undertaken in several studies. These studies generally employ feature recognition of a target from a database of images. These methods, though still premature and not yet ready to be flown in space, merit some discussion in their applicability to the problem at hand.

Feature recognition would allow a spacecraft to undertake precision maneuvers, as well as avoid potentially hazardous objects or situations. One drawback to many of these methods is that *a priori* knowledge of the object is assumed. However, if one is attempting to circumnavigate an unknown object, this presents a problem. More often

than not, detailed knowledge that would allow a database of features to be built is not available for adversarial assets.

A possible work-around to this *a priori* knowledge database would be to build a database in real-time. A method of determining a satellite surface using various basic geometrical shapes has also been proposed (16). Elementary shapes such as cones and cylinders delineate the primary features extracted from an image of a satellite's surface. The entire catalog of basic shapes is combined to render a dimensional model of the object. This method does have potential, but the technology is still primitive and not ready for implementation.

Aside from feature extraction and target modeling, range information is a prerequisite for determining proximity to a target. Though this paper will not undertake the task of determining an appropriate method of passive ranging, others have investigated the topic. A useful method of passive ranging has been proposed by Reilly, et. al. (22). The technique was developed as a method of ranging ships at sea. It uses triangulation methods to determine the data it collects from optical sensors working in the near-infrared range. The mechanism designed occupies a large space, as the optical sensors are placed approximately ten feet apart in order to range at distances of tens of kilometers. Though as of yet unproven for space application, this method holds promise, and would likely be the method of choice to add to a system such as the one proposed in this paper.

Thus the current efforts to aid in the rendezvous and/or tracking of a non-cooperative target show potential yet remain immature. A commercially available and established technology is desired in order to improve the chances of successful tracking.

2.3 Methods of Detection

Acoustic methods for detection generally center around pressure-measuring devices (8). Since there is essentially no medium with which to transport pressure waves outside of the earth's atmosphere, this class of measurement devices is quickly dismissed.

Potential measuring devices typically measure either a difference in the gravitational or magnetic potential of an object (8). Gravimeters and magnetometers can be well employed in space for attitude measurements with respect to the earth. However, the comparatively weak and overshadowed fields from a target satellite at relatively long distances are not a good match for these types of measurement devices. This class of device was thus dismissed.

Thus, the detector class of choice is electromagnetic. Even within this broad class, there are many different types of detectors. Detector selection inside this class must discriminate amongst imaging/non-imaging sensors, scanning/non-scanning sensors, as well as the trade-off between spatial, spectral, and intensity information. Certainly the portion of the EM spectrum that should be used is also of great importance.

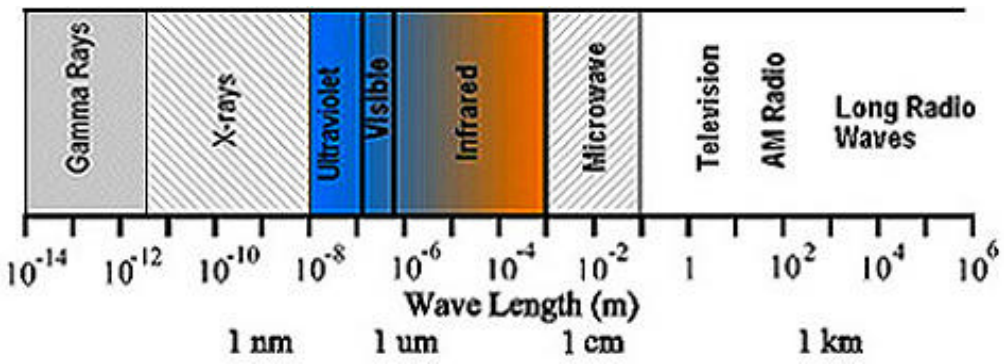

Figure 2. The Electromagnetic Spectrum

2.3.1 Electromagnetic Radiation

Perhaps the most apparent choice of EM energy to use is that of the visible spectrum. Optical cameras that operate in space have been used for many years with great success. Detection of a satellite could easily be measured by simply reading the output values from a camera's focal plane array to sense the presence of the object in the field of view (FOV). However, the immediate drawback to this is that the energy being absorbed is produced by the reflected light in the visible region of the EM spectrum. Once the light source is removed, reflection is also removed, and no image is available. This scenario is possible in the event of an eclipse, which, in the case of low-earth orbiting (LEO) satellites, is a frequent occurrence. Even in the case of geosynchronous (GEO) satellites, there are periods of eclipse which cannot be avoided. Thus, the decision to use a traditional optical camera in the visible portion of the EM spectrum is opted against.

Radiation-measuring platforms throughout all parts of the EM spectrum have been used successfully, though many are used only in specific applications due to the presence or absence of atmospheric constituents. The absorption characteristics of various constituents block the transmission of certain wavelengths. Though all other spectral regions (X-ray, UV, microwave, infrared, etc.) are available for use, not all are desirable. As outlined below, the majority of the radiation will be emitted in the infrared region, which makes it the more suitable choice for detection.

2.3.2 Infrared Radiation Characteristics

Any object with a temperature above absolute zero will radiate energy in some portion of the EM spectrum (8). The hotter an object is, the shorter the wavelength of its radiation becomes. For a blackbody, the law governing its emission of radiation (exitance) is Planck's Law

$$M(\lambda, T) = \frac{2\pi hc^2}{\lambda^5 (e^{ch/\lambda kT} - 1)} \qquad (1)$$

where

M = exitance (W/cm^2 μm)

λ = wavelength (μm)

c = 3*10^8 (m/s)

h = 6.626*10^{-34} (Js) (Planck's constant)

k = 1.38*10^{-23} (J/K) (Boltzmann constant)

T = object temperature (K)

For the analysis that follows, a simplified average satellite temperature of 300 K is assumed. Figure 3 shows a plot of the exitance versus wavelength for a body at 300 K. Integrating Equation 1 over all wavelengths, it can be shown that 90% of the total power emitted by a blackbody at 300 K lies in the wavelength region from approximately 7-45 μm (8). Thus it is desirable to focus on emission in the infrared portion of the EM spectrum.

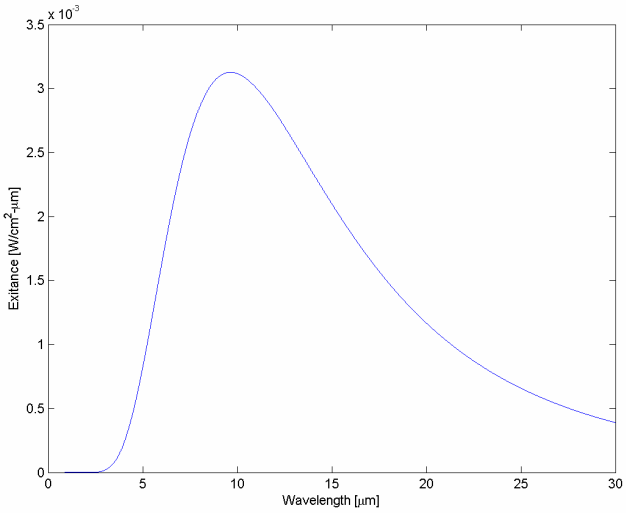

Figure 3. Radiant Exitance for a Blackbody at 300K (7)

Furthermore, Wien's Displacement Law can be examined to determine the peak wavelength of emission. Wien's Law is written as

$$l_{\max} = \frac{2897 mm \cdot K}{T} \quad (2)$$

where $l_{\max}$ represents the wavelength of maximum exitance. For a body at 300 K, this value is approximately 9.66 μm. Thus from the various spectral regions available for use as detecting mechanism, the best choice is the infrared region. The infrared region is typically broken up into the near-infrared (~0.7 – 1.1 μm), the medium wave-infrared (MWIR) (~1.1 – 7 μm), and long wave-infrared (LWIR) (~7 μm – 1mm). Thus, a LWIR camera is best suited for this task.

With the method of detection chosen, the method of measurement must be determined. There are many possible options for the materials and mechanisms used in infrared detection, and several options will be explored.

2.4 Infrared Detector Selection

Infrared detectors are generally broken into two main classes—photon and thermal (4). The division between the two is inherent in the manner in which each class measures the radiation incident upon it. Thermal detectors, which were the earliest to be invented, have their temperatures changed by the incident radiation, and some temperature-dependent property of the material is then measured (4). A familiar example of a thermal detector is the common thermometer. Other types of thermal detectors are bolometers, Golay cells, and pyroelectrics. Thermal detectors have seen a resurgence in their popularity in recent years with the advent of materials with shorter thermal time constants which allow the use of two-dimensional focal plane arrays (4). Common thermal detectors can provide a noise-equivalent temperature difference (NETD) as low as 40 mK with F/1 optics (4). Thermal detectors are advantageous in that they can operate at room temperature (i.e. no thermoelectric or cryogenic coolers are required), but carry the unenviable properties of being slow to respond to changes in radiation, and relatively insensitive (4).

The other class of infrared detectors was brought about by the desire to improve upon the disadvantages of the thermal detector. Photon detectors use materials that directly absorb the incident radiation and alter the atomic association of the material. The material may then change its inductance, voltage, or current in response to this, which is in turn measured by some attached meter. Common photon detectors in the visible portion of the EM spectrum are primarily based on Silicon and its alloys. In the infrared range, mercury cadmium telluride (MCT) is currently the most significant detector (4). Photon detectors are much more sensitive than thermal detectors, and can respond to

changes in infrared radiation much more quickly. Unfortunately, these require cryogenic cooling in order to reduce the dark current, which is the key to achieving such sensitivity.

It is this last disadvantage of photon detectors that generates cause to eliminate them from this study. Aboard a microsatellite, the addition of any extraneous device is costly both in terms of weight and power. Therefore, the detector of choice in this study is a thermal detector.

Furthermore, the receiving camera should utilize a two-dimensional focal plane array, or "staring" configuration. This configuration allows each individual detector that comprises the array to always be looking out in space. Optional configurations would be a single detector which scans the entire field of view, or a linear array which scans the field of view line-by-line. These latter configurations are disadvantageous in that they require extra mechanical parts in order to focus the detector at another portion of the field of view, as well as the fact that they require much faster response times. Selection of a two-dimensional array supports the selection of a microbolometer in that the slow response time of the microbolometer is negated.

Though conventionally a standard property that is used in the selection of an infrared detector is the noise-equivalent temperature difference (NETD), this performance characteristic was not deemed necessary in this analysis. Due to the "low-tech" nature of the mission, a very low NETD was not considered important. The reasoning should more become apparent in the experimental description. According to Wood (4), a good-quality infrared image requires an NETD of 300 mK or less. Most commercially available detectors should meet this restriction.

The size of the focal plane array is important, but not a limiting factor. Because the intent of the image received by the camera is simply for targeting/tracking purposes (and not identification), detailed imagery is not necessary. For long-range viewing, a larger array is desirable for a finer distinction of the target. Strides towards larger arrays (640 x 480) are being made quickly. A size suitable for operational use today is approximately 240 x 240 (4), though larger arrays are certainly possible.

The specific type of thermal detector to be used is not readily apparent. Pyroelectrics and bolometers both seem to offer their own advantages and disadvantages. Whatmore and Watton (4) suggest that a resistance bolometer offers better responsivity than pyroelectrics, but carries with it slightly higher noise. For this analysis, a microbolometer-based system was chosen, simply because they were more familiar to the author. Microbolometers are readily available in commercial-off-the-shelf (COTS) cameras.

2.5 Infrared Modeling of Target Satellite

What follows is the mathematical justification for using an infrared camera to detect the presence of another satellite in space. Several simplifying assumptions have been made. The target spacecraft will be represented as a cube with a surface area of 1 m^2 exposed to the imager with a viewing angle of zero degrees. The target will be assumed to have an average temperature of 300K (11). The standoff distance used for calculations is a conservative 1000 m.

It remains to be shown that the proposed method of detection is a viable one. One manner in which to prove this is to calculate the maximum detectable range of a

particular source, as outlined by Dereniak and Boreman (7). This method assumes that the background noise is not the limiting factor in the detection, and hence a non-background-limited infrared photodetector (non-BLIP) derivation is used.

The equation which defines the maximum range at which a point source can be detected is (7)

$$r = \sqrt{\frac{D^*}{\sqrt{A_d \Delta f}} \frac{I \times A_{enp}}{SNR}} \tag{3}$$

where

r = range

SNR = signal to noise ratio (dimensionless)

I = source intensity (W/sr)

A_{enp} = area of entrance pupil of collector (cm^2)

A_d = area of detector array (cm^2)

Δf = noise equivalent bandwidth (Hz)

D* = normalized detectivity ($Hz^{1/2}cm/W$)

D* represents a detector's sensitivity normalized to a 1 cm^2 area and 1 Hz noise-equivalent bandwidth (7).

Assumed values were input into the equation, and a maximum detectable range of approximately 1480 m was computed (as detailed in Appendix A). This is more than adequate under the initial assumption. Thus, if a point source is detectable at such a range, an extended source will be visible form closer range.

A commercial-off-the-shelf (COTS) infrared camera that meets the above specifications is not difficult to find. Several manufacturers make uncooled microbolometers with the range to accommodate the proposed dimensions. One such company is Indigo Systems. Indigo produces several lines of uncooled infrared cameras. One model suitable for application is the Merlin. Its nominal range extends to 1000 meters, is equipped with a 320x240 element detector array, and weighs in at just 3.5 pounds (13). If one could guarantee closer orbital flight of the target, the Omega model weighs only 120 grams (without a lens) and can image out to 300 m.

Figure 4. Indigo Systems' Merlin (left) and Omega Bolometer Cameras

Two obstacles remain in the unfettered detection of an object at in space at the proposed temperature—the degradation of the image by background radiation from both the Sun and the earth. Neither will be in the background of the image at all times, but both will share a spot in the background at some point throughout the orbits. Will either source prove to be a difficulty in the detection algorithm?

Detailed models of the IR radiation of the earth are difficult to obtain. The most comprehensive analysis to date has been the Earth Radiation Budget Experiment (ERBE) conducted by NASA. The term Earth Radiation Budget (ERB) denotes the overall

balance of radiation retained and emitted by the earth. An intensity map of earth's emitted longwave radiation at the top of the atmosphere (6408 km) is shown in Figure 5.

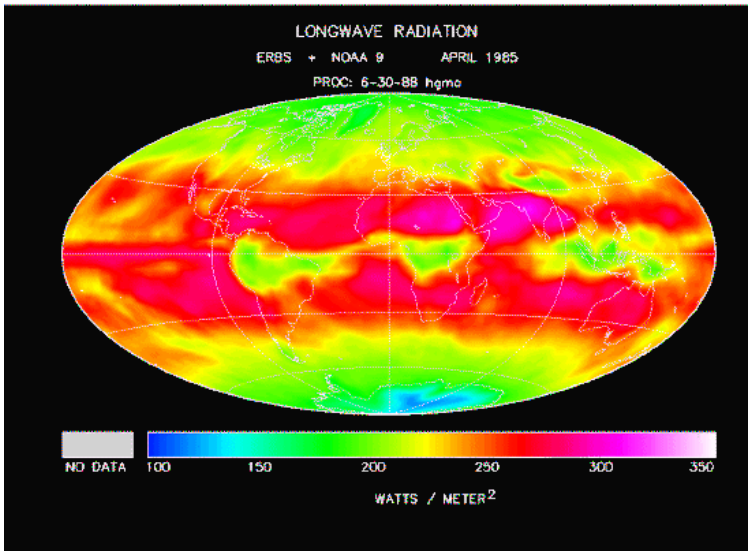

Figure 5. Intensity Map of Top-of-Atmosphere Emitted Longwave Radiation

Gilmore, et. al., (11) have compiled the data from the ERBE experiments which shows an average exitance of approximately 220 W/m^2 = 0.022 W/cm^2. This average value must be qualified with the information that the longwave interval established for the purpose of ERBE extends from 5-50 µm. The exitance of the notional satellite introduced above is calculated in Appendix A as 0.003504 W/cm^2, where the wavelength interval of interest for the theoretical detection scenario (8-10 µm), constitutes only approximately 5% of the total wavelength interval from ERBE. Furthermore, detection of the target is based upon total power received by the detector, which is a function of how much area is observed. If the observed area of the background (earth's atmosphere) is much larger than the satellite (a function of the range to target), more power will be let

in. In such a case, the image could appear inverse-video, in which case a robust code would have to switch its averaging properties.

At LEO, the earth fills the entire background of the image. At GEO, the earth is seen approximately as a 17° disc. An established capability such as an Earth sensor could be used to aid in the discrimination of image data should the need arise. Though traditionally used for coarse navigation purposes, a sensor could be used as a flag to alert a GEO satellite of possible erroneous image data.

The second, and less imposing, obstacle faced is the background radiation of the sun. The radiation emitted by the Sun is much better characterized than that of the Earth. Several sources including Elachi (9) characterize the Sun as a blackbody at approximately 5800K. Rees (21) provides a method of calculating the exitance in a specific spectral region as

$$\int_{l_1}^{l_2} M_l \, dl = s\,T^4 (f(x_1) - f(x_2)) \qquad (4)$$

where

$$x_1 = \frac{hc}{l_1 kT}$$
$$x_2 = \frac{hc}{l_2 kT} \qquad (5)$$
$$f(x) = \frac{15}{p^4} \int_0^z \frac{z^3 dz}{e^z - 1}$$

and z is a generic variable of integration. With λ_1=8μm and λ_2=10μm, f(x_1)=0.00124 and f(x_2)=0.00066. Then

$$M(8-10mm, 6000K) = 5.67 \cdot 10^{-8} \cdot (6000^4) \cdot (0.00124 - 0.00066)$$
$$M(8-10mm, 6000K) = 42620 W/m^2 \qquad (6)$$

This figure is four orders of magnitude greater than the previously determined output for a satellite in the same spectral region. However, workarounds are possible. If the solid angle subtended by the satellite is not great enough (i.e. range too large) to negate the irradiance from the sun, a sun sensor could be employed to discriminate the signals. Similar to an Earth sensor, a sun sensor could aid in the processing of the image data by filling a register indicating a certain percentage of the sun occupied the field of view. The data could be temporarily invalidated and control would continue in its current state until the offending presence was no longer detected.

The conclusion made is that an easily and commercially obtainable IR sensor could be employed for detection purposes even in the face of the aforementioned obstacles.

2.6 Orbital Dynamics of Close Spacecraft Formations

When considering close proximity operations, the relative motion between the two spacecraft is all-important. Hill studied the first development of the equations of relative motion in 1878 (28). The equations were re-derived in the 1960s by Clohessey and Wiltshire for more specific application in rendezvous. They are used to describe the linearized motion of a chase vehicle about its target. The Clohessey-Wiltshire (CW) equations are valid when one of the spacecraft (generally the target) is in a circular (or very near circular) orbit, and the second is "relatively close" to the first in the same orbital plane. Hill's equations are used when considering proximity operations of satellites, circumnavigation of a target, and rendezvous.

It should be noted that a method of arriving at the approximate relative distance is not covered in this paper. It is assumed that the maneuvers to achieve proximity have already been performed. For more on the close proximity arrival of the chase, see Tschirhart (26).

A brief overview of the concept of spacecraft relative motion is now given. For a more detailed analysis, several texts are available, including Wiesel (28) and Chobotov (5).

The standard equation of motion for a two-body system is

$$\ddot{\vec{r}} = -\frac{m}{r^3}\vec{r} \qquad (7)$$

where

$\vec{r}$ = position vector from mass 1 to mass 2

r = magnitude of the position vector

μ = gravitational constant of Earth (398601 km/sec^3)

The target satellite is assumed to be in a circular orbit, with radius (semi-major axis) equal to a. The target's mean motion is then $n = (\mu/a^3)^{1/2}$. A moving reference frame $[\hat{r}\hat{s}\hat{w}]$ is centered on the circular orbit about the target where $\hat{r}$ points radially outward from the target to the chase vehicle, $\hat{s}$ points along the direction of the reference frame's velocity, and $\hat{w}$ is normal to the orbital plane (see Figure 6).

Figure 6. Relative Frame of Target in Inertial Space

The chase vehicle is located at some distance from the center of the moving reference frame, nominally stated as $r\hat{r} + s\hat{s} + w\hat{w}$. Thus, in the relative frame, the overall displacement vector of the chase vehicle with respect to the target is

$$\vec{r} = (a + r)\hat{r} + s\hat{s} + w\hat{w} \tag{8}$$

The velocity and acceleration vectors can be found to be (25)

$$\begin{aligned} \vec{v} &= (\dot{r} - ns)\hat{r} + [\dot{s} + n(a + r)]\hat{s} + \dot{w}\hat{w} \\ \vec{a} &= [\ddot{r} - 2n\dot{s} - n^2(a + r)]\hat{r} + [\ddot{s} + 2n\dot{r} - n^2 s]\hat{s} + \ddot{w}\hat{w} \end{aligned} \tag{9}$$

Substituting this acceleration term in the two-body equation of motion, the Clohessey-Wiltshire equations of motion can be found to be

$$\begin{aligned} &\ddot{r} - 2n\dot{s} - 3n^2 r = 0 \\ &\ddot{s} + 2n\dot{r} = 0 \\ &\ddot{w} + n^2 w = 0 \end{aligned} \tag{10}$$

The C-W equations can be parameterized in several manners. One method is outlined by Irvin (14) which leads to the parameterized versions of the C-W equations as

$$
\begin{aligned}
r &= r\sin(nt + b_o) + c \\
s &= 2r\cos(nt + b_o) - \frac{3}{2}nct + b \\
w &= mr\sin(nt + b_o) + 2qr\cos(nt + b_o)
\end{aligned}
\tag{11}
$$

where

$$
\begin{aligned}
b &= \frac{ns_o - 2\dot{r}_o}{n} \\
c &= \frac{2\dot{s}_o + 4nr_o}{n} \\
r &= \sqrt{(r_o - c)^2 + (\frac{\dot{r}_o}{n})^2} \\
m &= \frac{\dot{w}_o\dot{r}_o - w_o n^2(c - r_o)}{\dot{r}_o^2 + n^2(c - r_o)^2} \\
q &= \frac{w_o\dot{r}_o n + \dot{w}_o n(c - r_o)}{2[\dot{r}_o^2 + n^2(c - r_o)^2]} \\
b_o &= \tan^{-1}[\frac{n(r_o - c)}{\dot{r}_o}]
\end{aligned}
$$

As denoted by Irvin (14), c must equal zero, or else the second term in the equation for s would grow unbounded, and the model would quickly deteriorate.

Irvin further illustrates the relative orbit of the chase vehicle about the target by manipulating Equations (11). Assuming that the chase vehicle is in the orbital plane of the target, the resulting path traced out by the chase vehicle around the target in one full orbit about the earth is a 2x1 ellipse (see Figure 7). This case is referred to as the Centered In-Plane Ellipse (CIPE) case by Tragesser and Lovell (17).

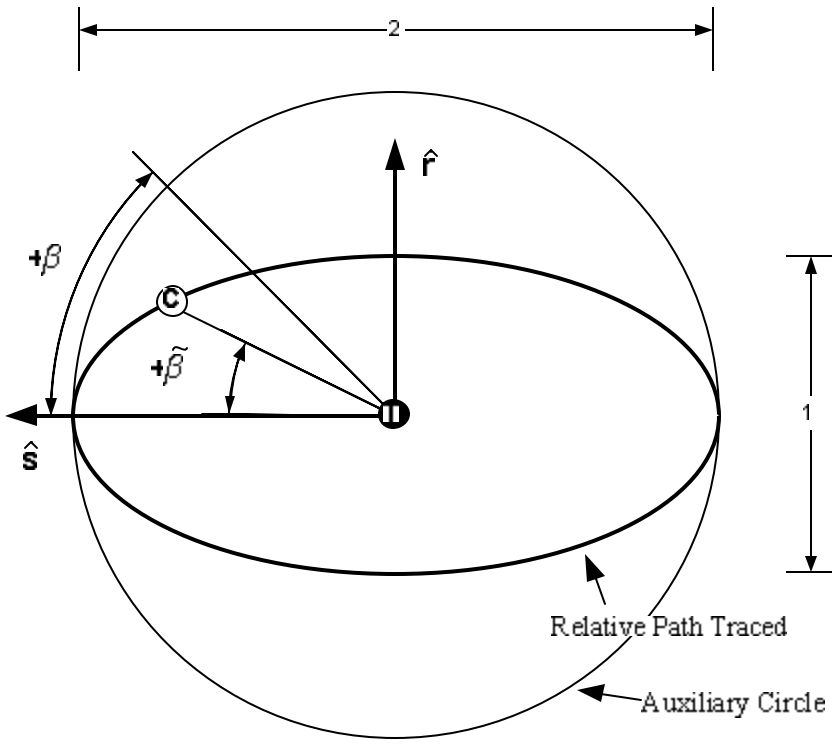

Figure 7. Chase Vehicle Motion in Target Relative Frame

In summary, Chapter II has shown that a commercially available infrared sensor is a viable means for the detection and tracking of a satellite in space. It was also shown that the path traced by the chase vehicle in the relative frame of the target is an ellipse. This information is furthered in Chapter III with the setup of the experimentation portion of this study.

III. Experimental Setup

In addition to the hardware used to conduct the physical experiment, two software models were created using Simulink® in order to validate the proposed methodology. One model was used to examine the effects on orbit (LEO/GEO case), and the second was modeled to represent the laboratory conditions. This chapter describes the setup of both software models and the hardware used in the tests. It begins with the development of the necessary equation and algorithm which underlie these models.

3.1 Determination of Required Yaw Rate

Since the objective of the chase vehicle's orbit is to maintain it staring at the target at all times, it must rotate throughout its orbit to do so. No rotation on the part of the chase satellite will only allow the target to be in its field of view for approximately half of its orbit. It must rotate at a differential rate so that it is spinning faster when it is in the wider portions of it relative path about the target. A central precept to note in the following derivation is that the chase vehicle is undergoing unforced motion.

The components of the chase vehicle's path in the $[\hat{r}\hat{s}\hat{w}]$ frame can be expressed as

$$\begin{aligned} r &= r\,\sin(nt + b_o)\hat{r} \\ s &= 2r\,\cos(nt + b_o)\hat{s} \end{aligned} \qquad (12)$$

The current angle $\tilde{b}$ can then be measured as

$$\tilde{b} = \tan^{-1}\left[\frac{r\,\sin(nt + b_o)}{2r\,\cos(nt + b_o)}\right] = \tan^{-1}\left[\frac{\sin(nt + b_o)}{2\cos(nt + b_o)}\right] \qquad (13)$$

Note the different angles b and $\tilde{b}$ in Equation 15 and Figure 7. The former is the true angle on the auxiliary circle. The latter is the angle within the ellipse. The two angles are not the same, and distinction between the two must be made. The rate that the chase vehicle must spin at is $\dot{\tilde{b}}$ in order to remain pointing at the target.

Taking the derivative of Equation 13 with respect to time yields the relative rate at which the chase progresses around the target. Using elementary calculus and introducing intermediate functions h(u) and z(t) facilitates the derivation. The arctangent and its components then take the form

$$h(u) = \tan^{-1}(u)$$
$$u(z) = \frac{f(z)}{g(z)} \tag{14}$$

By setting $f(z) = sin(z)$ and $g(z) = 2cos(z)$, the remaining functions can be related as

$$z(t) = nt + q_o$$
$$f'(t) = n\cos(nt + b_o)$$
$$g'(t) = -2n\sin(nt + b_o) \tag{15}$$
$$h'(u) = \frac{1}{u^2 + 1} = \frac{1}{\frac{f^2}{g^2} + 1} = \frac{1}{\left(\frac{\sin^2(nt + b_o)}{4\cos^2(nt + b_o)} + 1\right)}$$

The time derivative of $\tilde{b}$ can then be solved as

$$\dot{\tilde{b}} = h'(u)\cdot u'(z) = h'(u)\cdot\left[\frac{f'(z)\cdot g(z) - g'(z)\cdot f(z)}{g^2(z)}\right]$$

$$\dot{\tilde{b}} = \frac{1}{\left(\frac{\sin^2(nt+b_o)}{4\cos^2(nt+b_o)}+1\right)}\left[\frac{n\cos(nt+b_o)\cdot 2\cos(nt+b_o) - (-2n)\sin(nt+b_o)\cdot\sin(nt+b_o)}{4\cos^2(nt+b_o)}\right]$$

$$\dot{\tilde{b}} = \frac{2n\cos^2(nt+b_o) + 2n\sin^2(nt+b_o)}{\left(\frac{\sin^2(nt+b_o)}{4\cos^2(nt+b_o)}+1\right)\left(4\cos^2(nt+b_o)\right)}$$

$$\dot{\tilde{b}} = \frac{2n}{1+3\cos^2(nt+b_o)} \qquad (16)$$

Since $\dot{\tilde{b}}$ expresses the rate at which the chase satellite is moving about its target in the target's relative frame, it must also be the same rate at which the chase satellite must turn if it wishes to have the same orientation with respect to the target throughout their orbits.

3.2 Determination of Image Plane Centering Algorithm

In order to determine the actual angular offset present between the target and the center of the image plane, a simple algorithm based on the first moment of mass property was established. The algorithm uses the unsigned eight-bit (uint8) integers output from the camera and searches for the area of the image with the highest average white (pixel value equal to 255) value. A basis for this algorithm is found in Ginsberg (12). The

usage of uint8 data in this derivation is for two reasons: 1) this is the format used by the equipment in the laboratory, and 2) this datatype is very easy to manipulate.

In a physical mass, the center of mass is found by summing the individual moments from each contributing element about some point, and then dividing by the total mass. This process is repeated in each of three dimensions in order to locate the overall center of mass.

In this algrorithm, the reference point is the (1,1) element in the top left pixel of the image. The image plane consists of a 480x640 matrix of pixel values. The x-direction is considered to be in the horizontal direction; this equated to the column number of the pixel matrix. The y-direction is in the vertical direction, and thus corresponds to the row number of the pixel matrix. The "total mass" of the image is obtained by summing the individual pixel values over the entire image

$$m_{total} = \sum_{\substack{i=1 \\ j=1}}^{\substack{j=640 \\ i=480}} m_{ij} \qquad (17)$$

The center of mass in the either direction can then be found by dividing the analogue moment arm by the total "mass" of the system

$$X_C = \frac{\sum_{\substack{i=1 \\ j=1}}^{\substack{j=640 \\ i=480}} m_{ij} X_{ij}}{m_{total}} \qquad (18)$$

$$Y_C = \frac{\sum_{\substack{i=1 \\ j=1}}^{\substack{j=640 \\ i=480}} m_{ij} Y_{ij}}{m_{total}}$$

where X_{ij} is the column number of each pixel and Y_{ij} is the row number of each pixel. The X_C and Y_C coordinates then yield the pixel with the highest average intensity. The camera's field of view is then used along with an assumed range in order to determine the true angular offset. This algorithm was chosen due to it simplicity and high reliance.

3.3 Software Modeling of Test Cases

The software models were developed using Simulink. Simulink was the software package of choice due to its ease of use and ability to integrate with the other software packages used in the laboratory (Matlab® and dSPACE® ControlDesk®). In conjunction with the Real Time Workshop (RTW) package from the Mathworks, Inc., model compilation and implementation on hardware in-the-loop demonstrations is efficient.

The two software models were very similar. The theoretical case (space-borne) model calculates the difference in inertial positions of both satellites and converts them to an angular offset in the relative frame of the target. (All Simulink models are given in Appendix E.) The equations which model the motion are standard two-body equations of motion accounting for the J_2 perturbation. In the theoretical model, the chase vehicle was assumed to be in the orbital plane of the target, and at an initial distance of 100m in the direction of travel ($+\hat{s}$). The model for the theoretical case is shown in Figure 8.

Due to laboratory limitations, full motion of a two-body system could not be undertaken. Therefore, compromises in the modeling and experimental setup were made. The standoff distance and rotational period were changed in order to suit the lab environment. As the lab distances were fairly restricted, the distance to target was only 7

feet (2.1 meters). Additionally, in order to better view the motion of the satellite and target, a rotational period of the satellite of 800 seconds was chosen. Furthermore, the feedback loop that differenced the predicted motion and current motion was removed and replaced with an input from the centroid algorithm. The angular difference inputs were computed using a 17º field of view of the camera, and a seven foot range to target. Figure 9 shows the modified model for the laboratory.

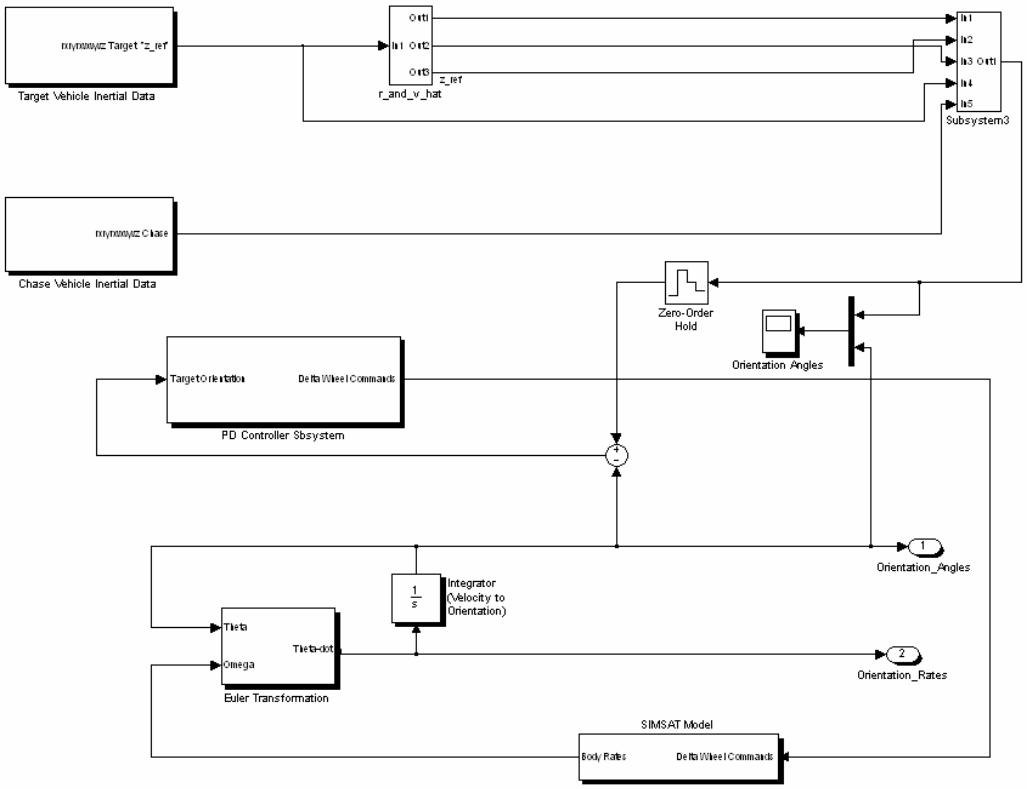

Figure 8. Simulink Model Simulating On-Orbit Motion

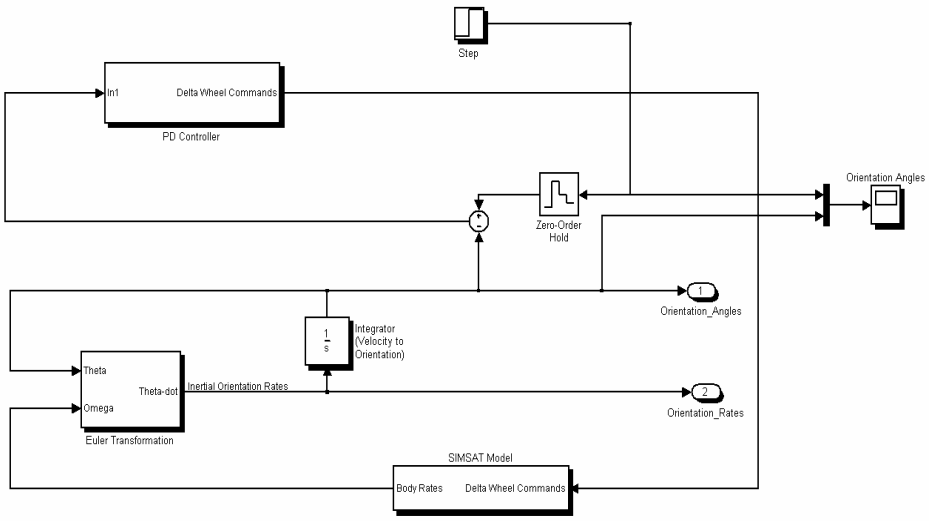

Figure 9. Simulink Model Simulating Laboratory Conditions

3.4 The SIMSAT

AFIT's simulated satellite (SIMSAT) was the hardware on which all tests were run. The SIMSAT was constructed in 1999 as a Master's thesis by several AFIT Systems Engineering students. The satellite weighs approximately 250 pounds, and has approximate dimensions of 6 feet (along the roll axis) by two feet by two feet (see Figure 10). SIMSAT uses three gyros for orientation sensing purposes, and both reaction wheels as well as a rudimentary CO_2 thruster system for orientation control purposes. It houses an onboard AutoBox® computer provided by dSPACE®. The AutoBox is the bed for the proprietary configuration cards onto which various software programs are loaded, and thus acts as the central processing unit aboard SIMSAT.

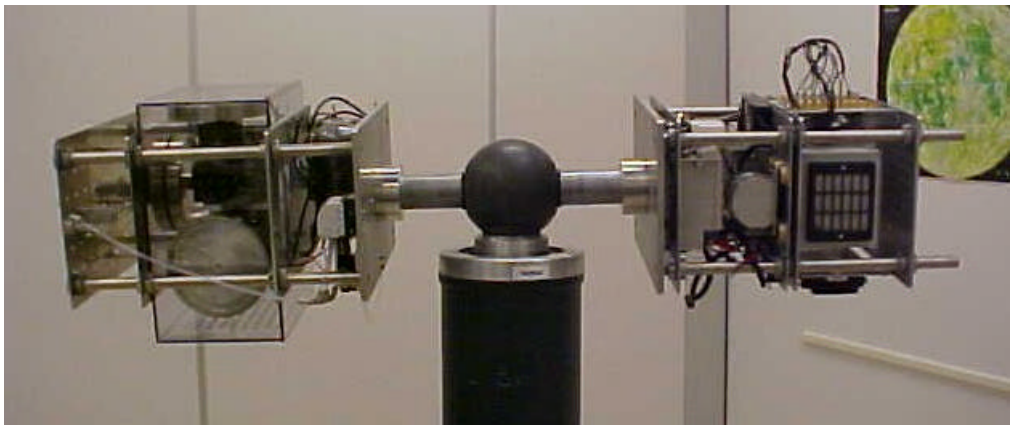

Figure 10. SIMSAT Atop Its Air Pedestal

A standalone PC houses the software which guides the operation of the SIMSAT. The PC utilizes MATLAB, Simulink, and ControlDesk by dSPACE in order to interact with the SIMSAT. ControlDesk is a hardware-on-the-loop control design program which can interface with most any test setup, and allows the user to create a custom graphical interface in which the pertinent design parameters can be monitored and manipulated. ControlDesk uses proprietary software to interact with Simulink.

The general setup used in this connection begins with a Simulink model of SIMSAT. It is processed and loaded to the AutoBox aboard SIMSAT via a wireless LAN connection. The custom graphical user interface is loaded and the experiment commences. Realtime commands and telemetry are shuffled between the standalone PC and the AutoBox aboard SIMSAT. Telemetry can be monitored and recorded, and various other parameters (such as satellite roll, pitch, and yaw) can be manipulated at will.

3.4.1 New Equipment

The hardware introduced for this experiment consisted of a near-infrared camera, a miniature color CCD video camera, an A/B audio/video (AV) switch, a wireless AV transmitter and receiver set, a lens piece, a high-pass optical lens filter, and a frame grabber. The new software introduced included the drivers for the framegrabber and the MATLAB Image Acquisition Toolbox. A list of specifications for all new hardware and software is included in Appendix C. Figure 11 depicts the satellite components attached to the +X-wing of SIMSAT.

The near-infrared camera is a COHU 4915 model, gray-scale CCD based camera. Its spectral range runs from approximately 250 nm to 1100 nm. A 2.5-cm lens was attached. In order to restrict the camera to the near-IR region for the experiment, a long-pass optical lens filter (750 nm and above) was appended to the standard lenspiece using rubber cement. The rubber cement allows for future removal and replacement of the filter without damaging the lenspiece, and eliminates the need for a separate lens holder to keep the filter abutting the lens.

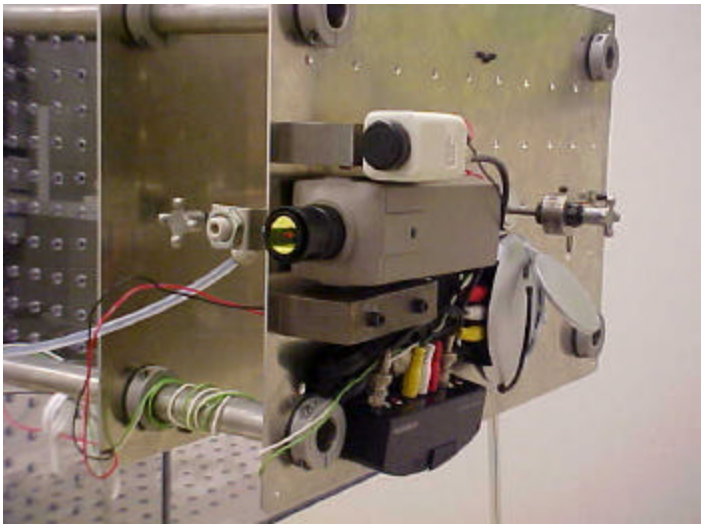

Figure 11. New Equipment Added for Experiment

The miniature color camera was attached simply for aesthetic reasons. A non-IR image may be desired in the future, and this will allow such functionality. The A/B AV switch joins both cameras, and the user can easily choose between which video feed is desired.

A wireless AV transmitter received the output of the A/B switch and sends the signal to the receiver which is located on a bench next to the stand-alone computer. The receiver sends its video signal into the framegrabber installed inside of the stand-alone computer.

MATLAB released its Image Acquisition Toolbox in May 2003. It works cohesively with certain model framegrabbers. The drivers for the framegrabber talk directly with the MATLAB, through which the user can control many different acquisition parameters, most notably the rate at which samples are taken in by MATLAB.

3.4.2 Hardware Experimental Process

Ideally, the entire process of image acquisition, image processing, and control algorithm computation would take place on the SIMSAT. Unfortunately, this was not possible due to several reasons. As mentioned before, the hardware and software associated with the dSPACE equipment is for the most part proprietary. The AutoBox computer aboard SIMSAT is not a PCI motherboard, and therefore will not accept typical framegrabbers. Thus, the image acquisition process was required to go through the stand-alone PC. A device was sought which might take the image straight from the camera and convert it to a grey-scale image data, thus feeding them directly into processor onboard SIMSAT. But the author had no luck finding any such device. The

process was then relegated to having the image acquisition and manipulation processes done on the stand-alone PC.

The process begins by invoking the Matlab code `main.m`. This code sets the timing for the entire transfer of data, and can be found in Appendix D. It initializes the framegrabber, prepares the video stream, and grabs the intermittent frames for evaluation. For each instance of an image grab, `main.m` calls a second file, `write2simsat.m`, which calculates the centroid of the image and writes the centroid pixel values to the ds1005 processor aboard the AutoBox.

The video stream processed by the framegrabber is collected through the wireless AV receiver. The individual snapshot frames from the Cohu camera are grey-scale image data (uint8 values). It was initially desired to transmit the data to the processor aboard SIMSAT and have the control algorithm processed aboard SIMSAT, thus making it feel a bit more realistic. After developing a custom MATLAB Executable (MEX) file in C language to perform this algorithm, it was discovered that the bit transfer rate of the RadioLAN system was not robust enough the required job. The transmission of a 480x640 matrix of integers would take too long via the wireless connection to facilitate any reasonable rate of control through image manipulation. Therefore, the process was again relegated to having the centroid algorithm run on the stand-alone PC as well.

The pixel value results from the centroid algorithm yield an angular offset from the view of the image plane. However, in order for this to be interpreted as an angle for the SIMSAT to slew through, the angle must be converted via geometry to an angle from the center of the SIMSAT. This angle is dependent on the location of the target, and is approximated in the Matlab code `write2simsat.m`. This angle is then transferred via

wireless link to the SIMSAT, where the Simulink model aboard the AutoBox implements the control scheme. Output telemetry is shipped over the wireless LAN and viewed using the ControlDesk software.

Obviously, the physical methods used to implement this scheme in the laboratory are not suitable for real world operations. On orbit, all calculations would have to be performed onboard the spacecraft. However, the computational process used in the laboratory is representative of the necessary process that would take place on orbit, therefore validating the laboratory setup.

IV. Experimental Results

4.1 Theoretical Case Solutions

The theoretical case involved two separate studies—one of a hypothetical polar orbiting LEO satellite, and one with real world data from a United States' asset. The orbital data used in the calculations is shown in Table 4-1. In both studies, the chase vehicle was assumed to be in the orbital plane of the target, and at an initial distance of 100m in the along-track direction ($+\hat{s}$). The LEO case will be discussed first.

Table 2. Orbital Data Used in Theoretical Simulations (31)

Orbital Parameter	LEO Case	GEO Case (DSCS III)
Semi-major axis, *a*	7000 km	42187 km
Eccentricity, *e*	0	0.0000399
Inclination, *i*	97.9°	14.3222°
Right Ascension, *O*	305.1º	351.98°
Argument of Perigee, *?*	N/A	268.4543°

4.1.1 Uncontrolled Case

Due to perturbations throughout the orbit (J_2 was the only one considered in this study) the path of the relative orbit "slips" some in the target's reference frame. An example can be seen in Figure 12. It is this slipping that causes a difference between the actual angle between the chase and target vehicles ($\tilde{b}$) and the modeled angle. If no perturbations were present, the model would match exactly and a closed-loop control

system would not be required. As it were, perturbations abound, and the problem must be solved by implementing some slightly more sophisticated type of control.

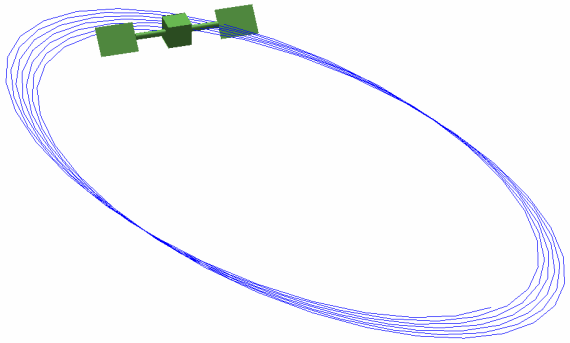

Figure 12. Depiction of Relative Path "Slip" Throughout 10-hour LEO Orbit

In the software models, the two-satellite systems were allowed to propagate for various amounts of time, culminating in a test case of 12 hours. In each case, the theoretical $\tilde{b}$ was differenced from the actual angular difference between the two satellites. The results of these calculations are shown in Figures 13 and 14. There is a significant difference between the LEO and GEO cases in total angular offset through the same period of time. Over the same time duration, the angular difference is much lower in the geosynchronous orbit. This is attributable to the greater effect that the J_2 perturbation has at lower orbital heights. The same pattern of oscillating error is seen in the GEO case, but several days are needed for the magnitude of the error to increase to the same levels as those seen in the LEO plot. The unbounded nature of the error in pointing angles necessitates the addition of closed-loop control.

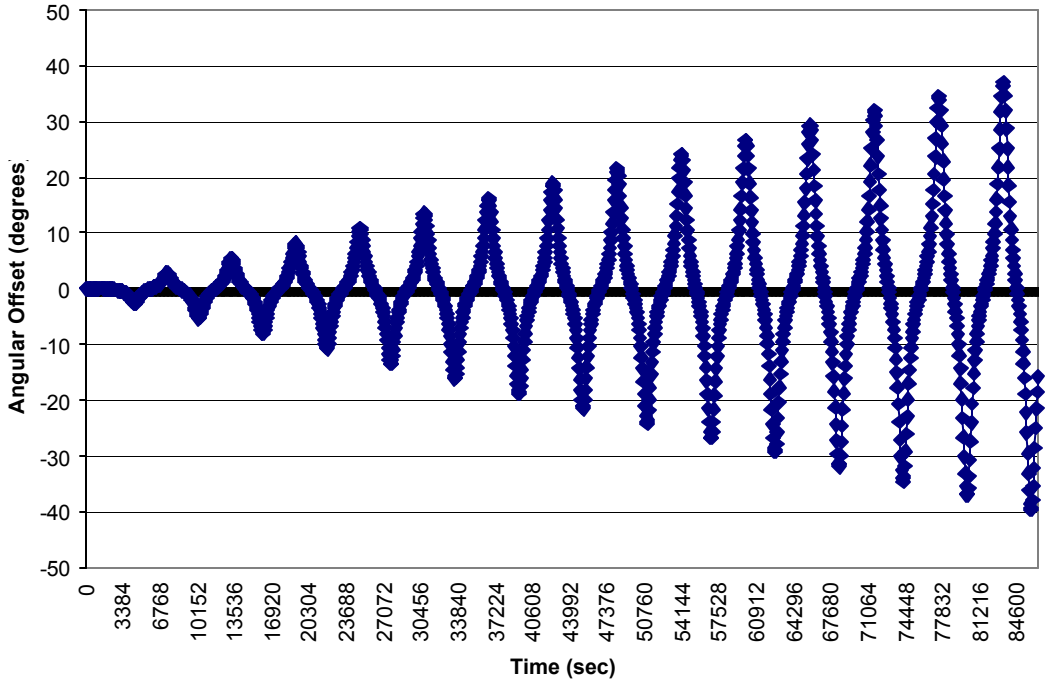

Figure 13. Angular Difference Between Modeled and J_2–perturbed Orbit LEO Case

Figure 14. Angular Difference Between Modeled and J_2–Perturbed Orbit GEO Case

4.1.2 Controlled Case

As a starting point for the closed-loop control, the nominal $\dot{\tilde{b}}$ was input to the system as a pseudo-feed-forward term. Additionally, a simple proportional-plus-derivative (PD) controller was developed to augment this foreknowledge. The resulting angular rotations plotted over time can be seen in Figure 15 for both the LEO and GEO cases. The plots of the perturbed motion and the controlled motion overlay each other very closely, making the traces indistinguishable at low resolution. A more insightful representation of the information is shown in Figure 16. These figures depict the differences in angles over time. Very good agreement is seen with the implemented control. Small angular differences between the "truth" (modeled J_2 movement) and the controlled spin of the satellite indicate a high ability for sustained tracking. When considering the angular offsets after only three hours, both the LEO and GEO cases have been improved by approximately 67%.

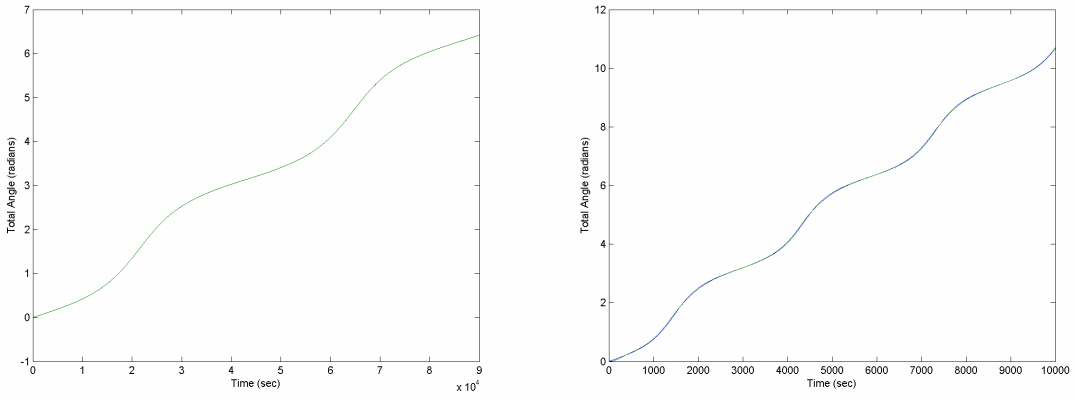

Figure 15. $\tilde{b}$ vs. Time for GEO (left) and LEO (right) cases

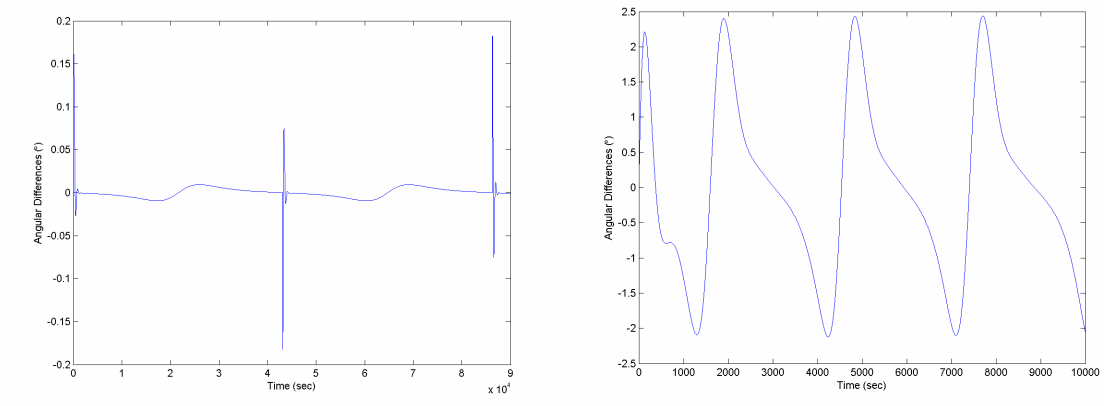

Figures 16. $\tilde{b}$ Differences vs. Time for GEO (left) and LEO (right) Cases

Because the trigonometric functions used return bounded values, the models were altered so that continuous values of total displacement were returned. Without this alteration, the values of the total displacement in Figure 15 would return to zero after reaching 2p and obstruct their interpretation. As such, the spikes in Figure 16 are a remnant of the momentary difference between the predicted and actual values. They should be ignored, as they do not represent the actual magnitude of the angular difference at these times.

Better overall agreement is seen in the GEO case. This is most likely due to the fact that the LEO case is in a polar orbit, and its response to the effects of the J_2 perturbation is much more prevalent.

4.2 Laboratory Results

The overall experiment consisted of three distinct portions. The first was to command the SIMSAT to follow the predetermined $\dot{\tilde{b}}$ as derived in Section 3.1. Tests In both the positive and negative yaw direction were conducted to average any bias in one of the directions. The second portion was to implement the tracking algorithm as developed in Section 3.2. Lastly, the two would be combined to track a moving target in the laboratory.

4.2.1 $\dot{\tilde{b}}$ Commanding

The orbital period of the satellite was replaced with a laboratory-friendly 800 seconds. Figure 17 shows the results of an initial test to command the SIMSAT to spin at the previously determined $\dot{\tilde{b}}$, along with the reported rate from the yaw gyro. The steady departure from the modeled turning rate indicated the presence of an additional unaccounted force. Previous SIMSAT enthusiasts had noted a similar disturbance. However, previous experiments did not have the same requirement for accurate angular reporting over such long time periods. Thus, a characterization of the supplemental disturbance was required.

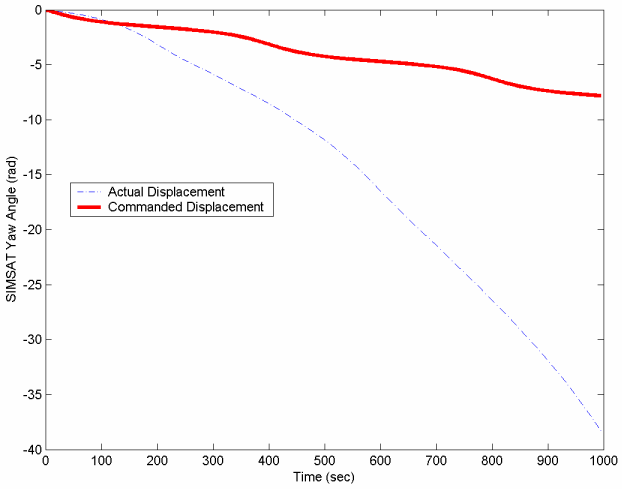

Figure 17. Initial Measurements of SIMSAT Body Yaw Rate with Forced $\tilde{\dot{b}}$

Several theories on the origin of the disturbance have been proposed such as exhaust air from the on-board computer, exhaust air escaping from minute separations between the air bearing and rotation sphere, and air currents from the building's ventilation system. It is the author's belief that the latter reasoning is the motive for the disturbance. Figure 18 shows the average time history of the (magnitude) increasing yaw rate. A first-order polynomial fit to the data was derived. This is also seen in Figure 18. This new information was placed back into the $\tilde{\dot{b}}$ model, and the same tests were executed. Unfortunately, this modeling did not improve the behavior of the satellite. Only marginal improvement over the initial model was seen. Figures 19 and 20 show the results of the model with the disturbance factored in, for both positive and negative commanded movement. Both plots show (noisy) pre-filtered gyro data. The use of pre-filtered data had no effect on the system.

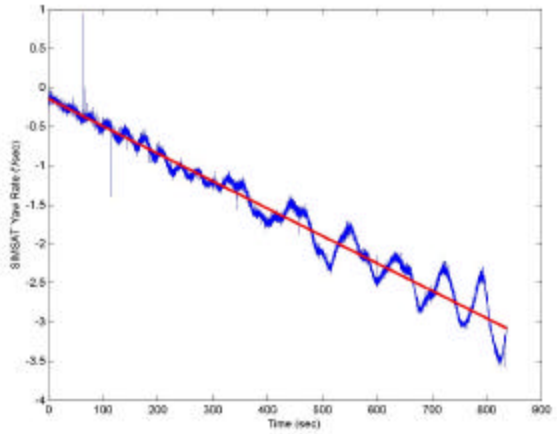

Figure 18. SIMSAT Unforced Acceleration: Average with Trendline

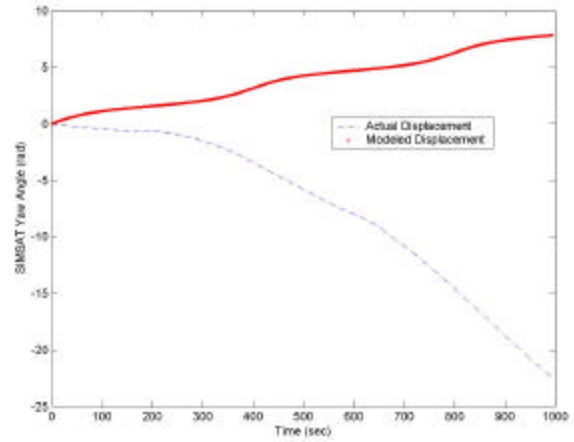

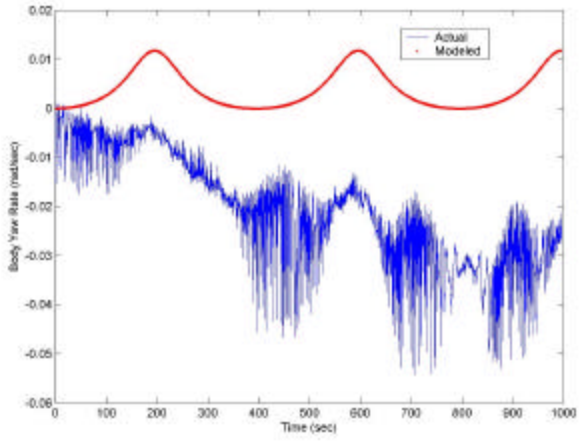

Figures 19. SIMSAT Yaw Angle and Rate vs. Time (Positive Case)

Figures 19 illustrate the total angular displacement traversed by the SIMSAT for a commanded yaw in the positive (top) and negative (bottom) directions, along with the expected angle.

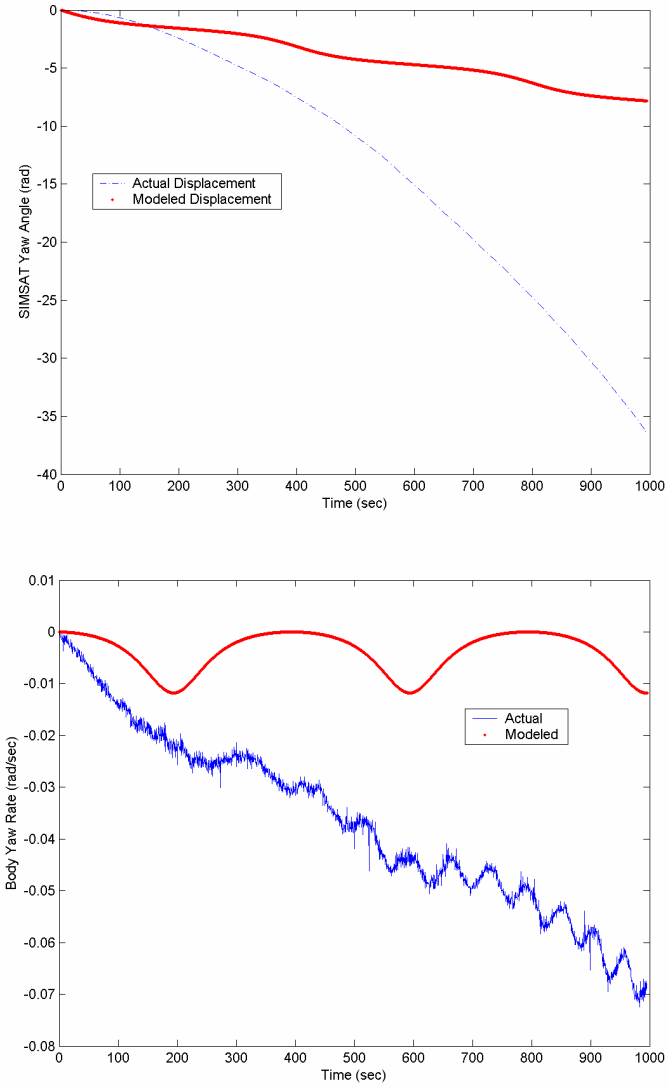

Figures 20. SIMSAT Yaw Angle and Rate vs. Time (Negative Case)

Figures 20 represent the same information for commanded yaws in the negative direction. Better overall matching is seen in the negative case because the additional disturbance is

geared in that direction. Lastly, Figure 21 illustrates the modeled yaw rate combined with the modeled disturbance as compared with the true rates for both positive (left) and negative (right) commanded yaws. The negatively commanded case provided the most accurate results, and so this was the only case chosen when attempting to track the moving target in Section 4.2.3.

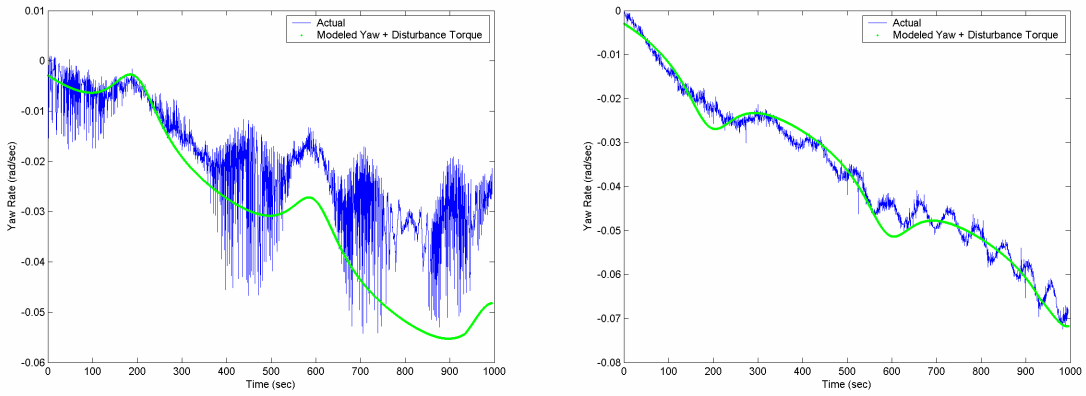

Figure 21. Modeled (with Known Disturbance) and Actual Yaw Rates

4.2.2 Infrared Camera Tracking of a Heat Source

This portion of the experiment attempted to show satisfactory tracking by the system of a step input. The step input was an initial offset of approximately negative five degrees from the center of the image plane (actual offset varied between three and eight degrees). Figure 22 shows typical open-loop images of the heat source (a AA battery flashlight) monitored, as returned from the near-IR camera.

Figure 22. Heat Source Moving Across the Image Plane over Time

A suitable controller was desired to handle the discrepancies noted in the previous section. It was determined that in addition to the PD controller designed in the theoretical case, a PI controller was necessary to account for this disturbance (20). Furthermore, the delay from the camera must now be taken into account.

The processing time for the pictures required about one second for each image. This included the time to perform the centroid algorithm as well as to write the subsequent data to the on-board computer. This delay was accounted for in the software model by adding a "Zero-Order Hold." The Simulink model for this system is shown in Figure 23. The results of the tracking tests are shown in Figure 24. The Simulink tests were given a step input of five degrees. As is seen, the Simulink model works very well, with minimal overshoot and acceptable settling time.

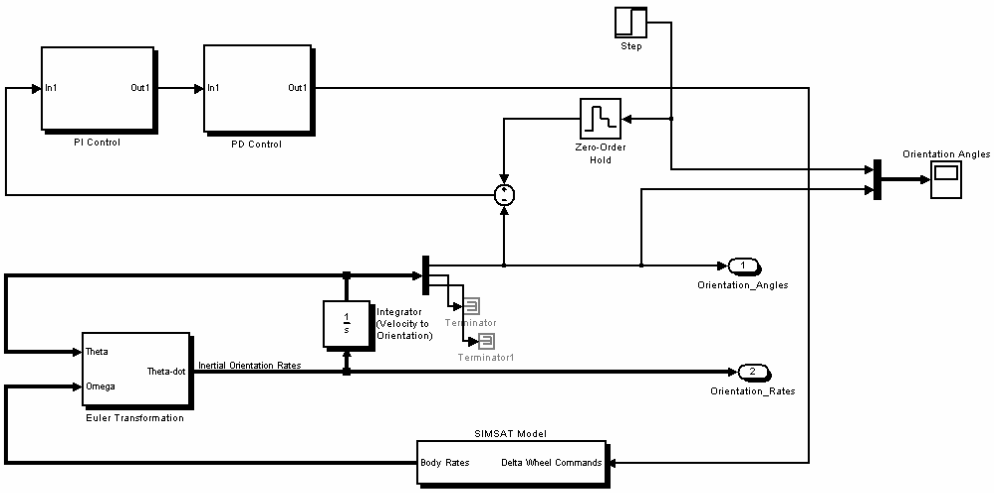

Figure 23. Simulink Model of SIMSAT System

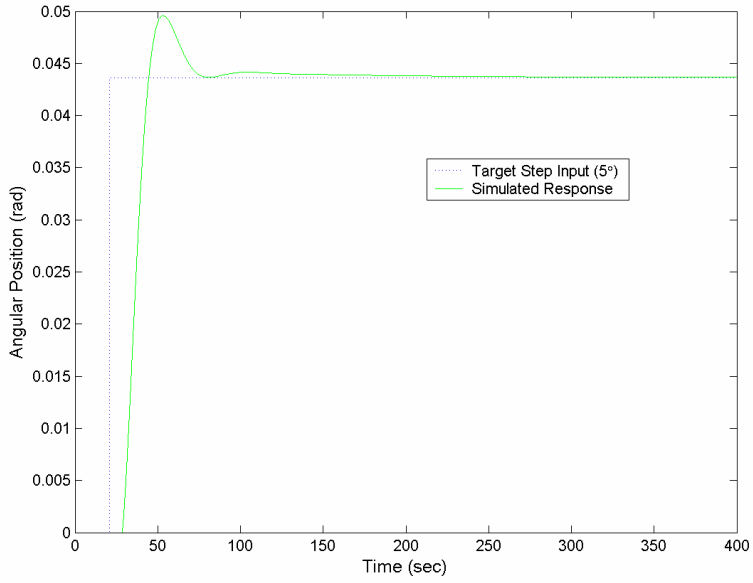

Figure 24. Closed-Loop Simulink Results for a 5º Step Input

Figure 25 shows the resultant yaw movement from two test cases—one "large" initial displacement in the positive direction, and one "small" initial displacement in the positive direction.

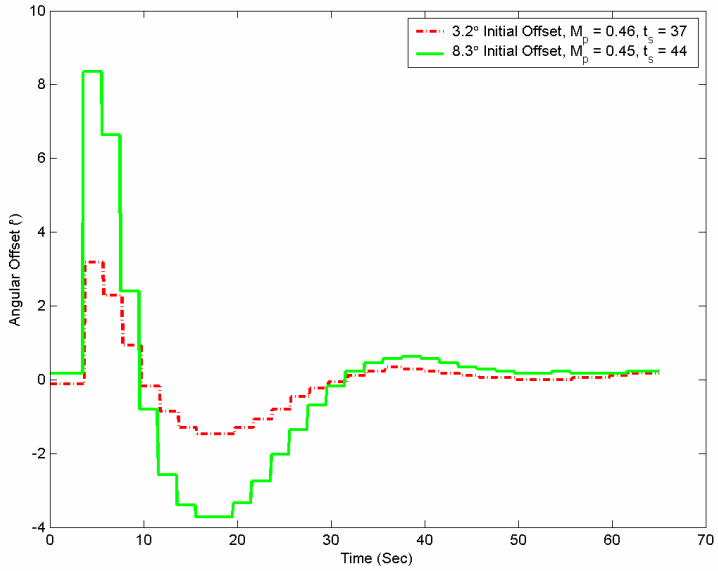

Figure 25. SIMSAT Step Input Behavior

Figure 25 is a graph of the commanded SIMSAT yaw angle as calculated by the centroid algorithm. This method of illustrating convergence is not the nominal method, but is the best alternative. The nominal method would be to show a plot of the inertial orientation yaw angle. Unfortunately, the gyro drift denigrates the true values, and shows non-convergence. For this reason, these plots were omitted from the results.

Also of note from Figure 25 is the lack of matching with the software model from Figure 24. The inconsistencies are overt, and attributed to a lack of sufficient understanding of the Animatics motors. It was not determined until late in the research effort that the motors behaved in a non-linear fashion and were subject to a PID

controller of their own. After discovering this, several attempts were made to tune this motor PID model to the application. The non-linear behavior of the motors necessitates that their PID controllers be tuned dependent upon the type of movement desired. In this particular effort, the acceleration constant in the Motor Initialization Routine of the Simulink model was set at 120 rad/sec^2. This allowed for acceptable (though non-optimal) convergence for the step input at moderately large angular offsets (between ±3° and ±10º). Smaller angular offsets (<±2º) can afford a larger value of the acceleration constant, and even larger slews can afford an even smaller acceleration constant.

4.2.3 Tracking of a Moving Heat Source

The difficulties encountered when trying to establish the first two portions of the laboratory experiment did not lay the foundation for a successful demonstration of tracking a moving target. Even so, the test was administered in order to glean information that might be helpful.

Figure 26 shows the Simulink model generated to model and predict the behavior of the hardware system before actual testing. As in the case of the stationary heat source (step input), the model tracks very well (see Figure 27). An intentional offset of five degrees was issue to the system to emulate unpredicted on-orbit disturbances. After adjusting to the input, the maximum separation between the two was approximately 2.5 degrees. Figure 28 shows the angular differences over a period of 1.25 rotations. The large spikes correspond with the addition and removal of the five degree offset.

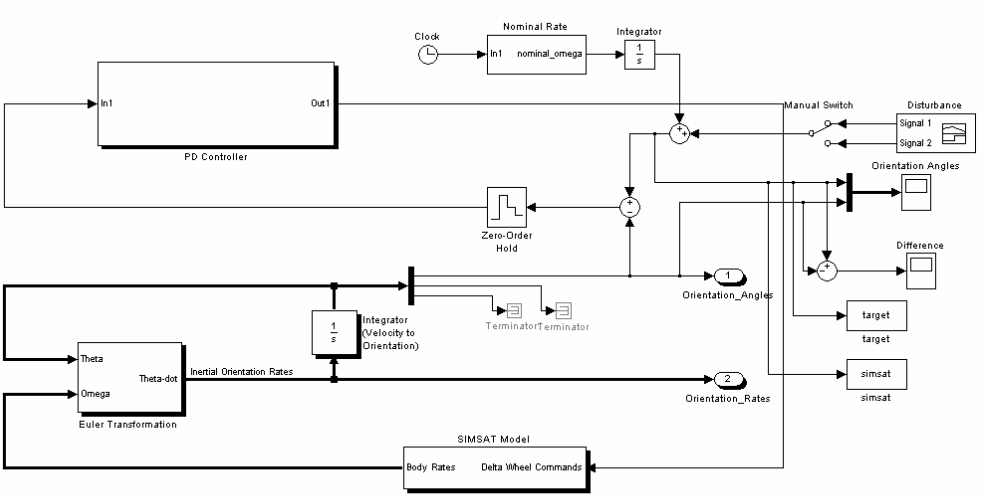

Figure 26. Simulink Model of SIMSAT System for Moving Heat Source

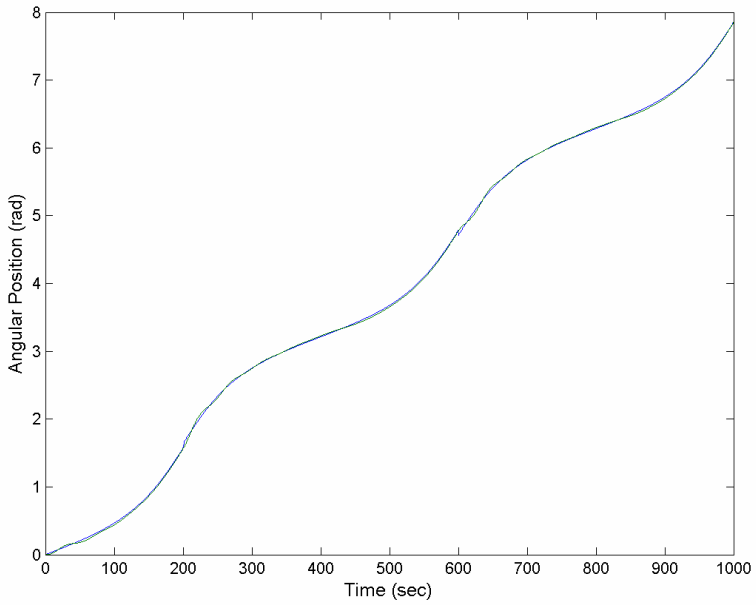

Figure 27. Closed-Loop Simulink Results for a Moving Heat Source

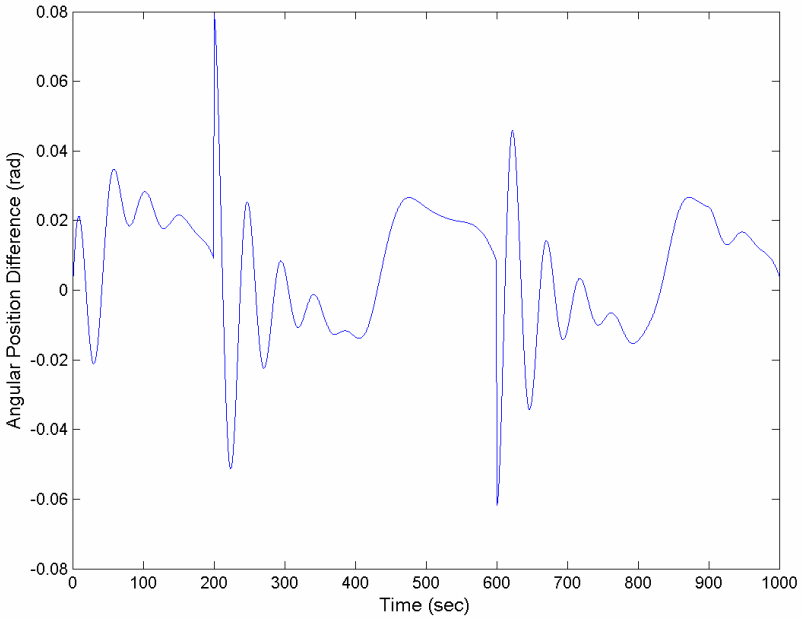

Figure 28. Angular Position Difference Between Heat Source and SIMSAT

The heat source was mounted on a wheeled chassis, which sat upon a track 30 inches in length. The camera's initial distance from the heat source was 84 inches. As time progressed, the flashlight moved in a linear manner, while the SIMSAT turned to maintain a track. The outboard positioning of the camera on the SIMSAT's +x wing required slightly different turning than what was predicted for. Ideally, the camera would have been mounted at the center of rotation of the SIMSAT, but this is not physically possible. A top view diagram of the hardware setup is shown in Fig 29.

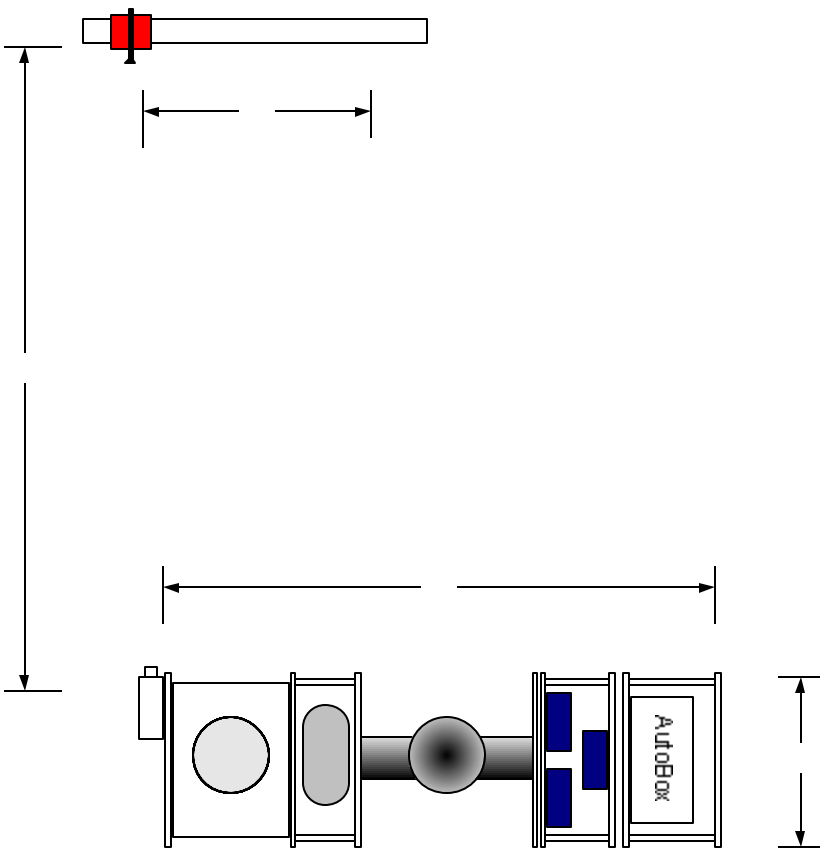

Figure 29. Top View of Hardware Experimental Setup

Due to laboratory limitations, complete rotation of the target about SIMSAT could not be undertaken, so a fraction of the entire orbit was emulated. The motion of the heat source in the nominal ellipse was modified to account for its linearly-restricted path on the track. Considering Equation 12 in conjunction with Figure 7, displacement in the $\hat{s}$ direction can be differentiated to yield the rate at which motion occurs in the cross-track direction as

$$\dot{s} = -2nr\sin(nt + b_0) \qquad (19)$$

The target was moved at the rate equal seen in Equation 19 for a period of 100 seconds. This replicates the movement of the target for only a portion of the full rotation, however it will yield enough information to allow justification of the model.

The experimental results from the moving target test are shown below in Figures 30 and 31. Figure 30 depicts the actual angular movement of the target, with the stars representing the offset as determined by the imaging algorithm. The difference between the two is the actual angular error and is shown in Figure 31.

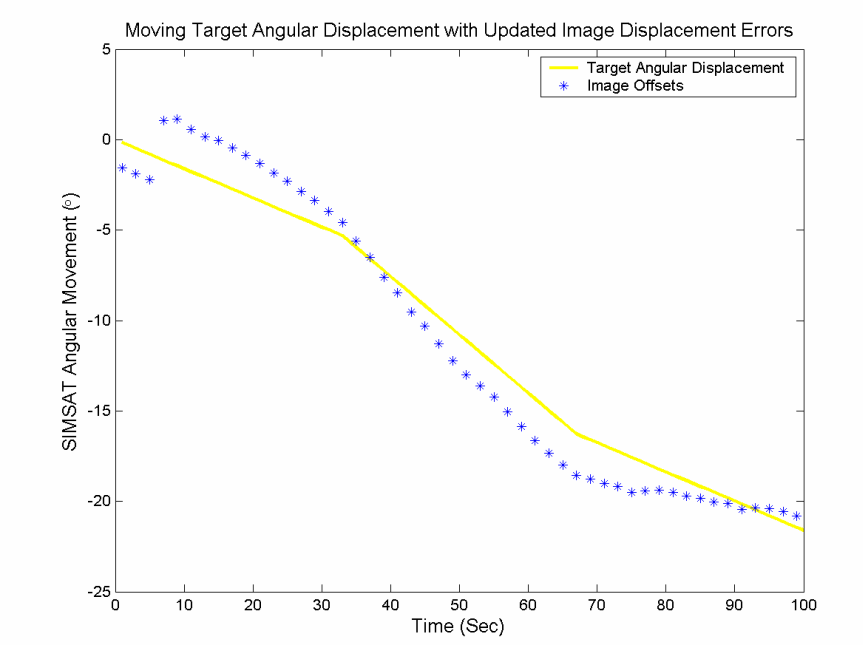

Figure 30. Results of Tracking Test with Moving Target and Integrated $\dot{\tilde{b}}$

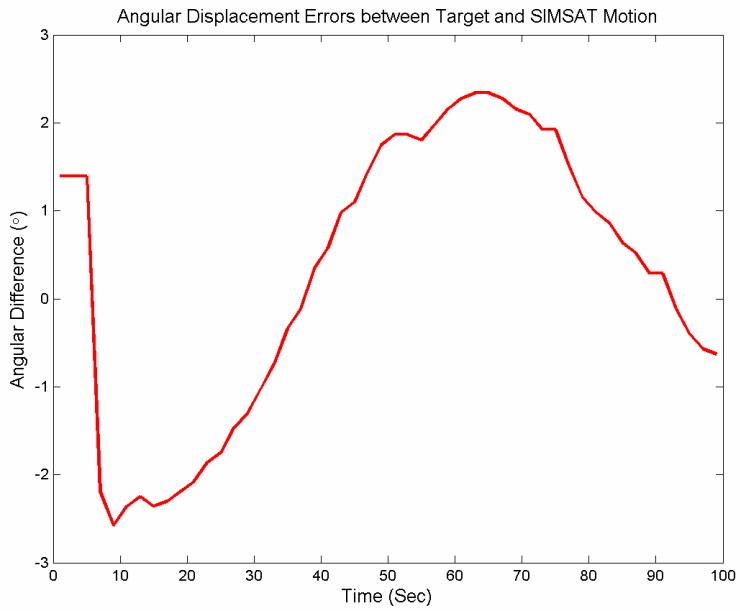

Figure 31. Angular Error Between Target and Image Calculation for Moving Target Test

In summary, hardware results successfully demonstrated the ability to track a moving target using updated image data from an infrared sensor. The controller values used were not optimized for the motor characteristics, and can afford further improvement. Successful demonstration in the lab environment justifies the previously developed on-orbit models and validates the final objective of the study.

V. Conclusions and Recommendations

5.1 Conclusions

The ability to completely characterize the surrounding environs of U.S. Space assets is not absolute. A degree of uncertainty exists as to the Space capabilities of U.S. antagonists. This study sought to determine some aspects of the possibility that an adversary might have a capability for autonomous loitering about and tracking of a target.

A brief discriminatory study investigated the possible options for remote sensing of a target satellite in close proximity. Different methods of detection were weighed and combined with information from previous and other on-going research in related fields. With a heavy prerequisite being passive detection, the choice of sensor was an infrared camera, a well-established and uncomplicated technology. Several criteria for infrared cameras were detailed in order to choose the most appropriate type. In the end, the most appropriate type of detector was found to be a microbolometer, as it offered the performance required with the benefit of not having to be cryogenically cooled. Many manufacturers were found to provide such a camera commercially.

Using a system outfitted with an IR sensor, a maximum detectable range of a 1 m^2 target satellite of approximately 1400 m was found. Indeed many commercially available microbolometer-based IR cameras today can meet this requirement.

The orbital equations of two close-orbiting bodies (Hill's Equations) were then explored to determine the mechanics of motion relevant to this scenario. It was found that for the in-plane, unperturbed case, the chase vehicle must rotate at a specified rate in order to maintain a stare at the target at all times. This specified rate is a function of the

angle between the chase and target satellites in the plane of the target. Introducing the J_2 perturbation caused the vehicles to depart from this specified angular relationship. The degree to which the angular differences diverge is a function of both orbital height and time. Thus a control scheme is required and was designed to reduce the error in the pointing vector.

The control scheme was modeled using both a proportional-plus-derivative controller alone as well as in series with a proportional-plus-integral controller. Over a flight duration of three hours, the PD controller reduced the magnitude of error by 67%.

Lastly, attempts were made to accurately model the motion and tracking of the two-body system in AFIT's SIMSAT laboratory. Non-optimal yet successful tracking of both a stationary and a moving target was demonstrated. Further tuning of the motor parameters is required to attain perfect software model-matching.

Some sources of laboratory error that prevented better agreement with the model include a disturbance torque, as well as non-linear motors. The motors are reasonably well-characterized, though some improvement could be made. Their non-linear behavior makes modeling them difficult, but the end results would be more than justified. The disturbance torque that is probably a result of the air currents in the room was also well-modeled, but future SIMSAT operations could benefit from further study of this phenomenon.

This work has shown that with few resources and no cutting-edge technology, a satellite subsystem can be designed that would allow a vehicle to passively orbit about and track a target satellite. The assembly and integration of COTS sensors and processors would not be difficult for an organization with rudimentary skills and abilities.

The orbital mechanics of the problem are relatively easy to derive, and the control implemented could be designed and even improved by a person or team with modest knowledge. With some further revision, the technique presented could be employed in a simple satellite system to solve one aspect of the problem of passive circumnavigation.

5.2 Recommendations for Future Study

Areas of study that are directly relevant to this work but were not investigated include the following:

- Passive ranging in Space
- Responses to detected target orbital maneuvers
- Autonomous acquisition of the target

Each of the above topics would shed great light on the capabilities of both friendly and hostile forces.

Several items of interest arose during the course of experimentation which warrant further investigation. They are as follows:

- Further characterization of the Animatics® motors should be accomplished. An acceptable model has been in place over the past three studies, but a more accurate model is definitely attainable. Accurate software modeling is impossible without a rigorous characterization of the motors.
- Investigate the possibility of using only the color CCD camera for image acquisition. The CCD used in the color camera may have the same spectral sensitivity as that of the COHU. If so, the COHU could be removed, freeing up space and removing a small amount of weight.

- Further characterization of the disturbance torque should be undertaken. A controlled environment must be established and all variables accounted for.
- Investigate new software options for the control and interface of the SIMSAT. The current software (dSPACE) may well be a powerful tool, but the learning curve, in combination with its propensity to spontaneously reject seemingly valid commands, make it difficult to exploit in the short time periods of study.
- Further investigate the possibility of obtaining a specific card for the AutoBox that will convert the image data onboard the SIMSAT.

Appendix A: Calculation of Maximum Range for Detection

The equation for detecting the maximum range at which a point source is visible in a non-background-limited infrared photodetector scenario is given in Dereniak and Boreman as

$$r = \sqrt{\frac{D^*}{\sqrt{A_d \Delta f}} \frac{I \times A_{enp}}{SNR}} \qquad \text{(A-1)}$$

where

r = range

SNR = signal to noise ratio (dimensionless)

I = source intensity (W/sr)

A_{enp} = area of entrance pupil of collector (cm^2)

A_d = area of detector array (cm^2)

Δf = noise equivalent bandwidth (Hz)

D* = normalized detectivity ($Hz^{1/2}cm/W$)

D* represents a detector's sensitivity normalized to a 1 cm^2 area and 1 Hz noise-equivalent bandwidth (7).

For this theoretical calculation, several values were assumed given a range of typical values also taken from Dereniak and Boreman. The values chosen were (for a thermistor bolometer operating at 300 K)

D* = 5 x 10^8 ($Hz^{1/2}cm/W$)

Δf = 1/(2t) = 1/(2*0.005 sec) = 125 Hz

A_d = 0.01 cm^2

A value of 2.5 was chosen for the SNR, as this was a common value amongst several examples throughout Dereniak and Boreman. The area of the entrance pupil was taken as 4p cm^2.

The value of intensity was calculated by initially assuming an average temperature of the target satellite of 300 K. The visible area of the source (target satellite) was taken to be 1 m^2. A conservative average emissivity (e) of the satellite is taken as 0.5, taking into account various values for the emissivity of Kapton insulation, GaAs or Si solar arrays, and painted surfaces of the target (website or Satellite Thermal Engineers Handbook). The target is assumed to act as a graybody radiator.

Integrated values for blackbody exitance at 8 μm and 10 μm were taken from Appendix A of Dereniak and Boreman. The values were then subtracted to yield the blackbody exitance (M_{black}) between 8-10 μm as 0.006108 W/cm^2. The source exitance was found by including the emissivity of the source as

$$M_{source} = eM_{black} = 0.5 * 0.006108 \frac{W}{cm^2} = 0.003504 \frac{W}{cm^2} \qquad \text{(A-2)}$$

Assuming a planar Lambertian emitter, the radiance, L, is related to the exitance by M = p*L (7). Thus the radiance is found to be

$$L = \frac{M}{p} = 9.721 * 10^{-4} \frac{W}{cm^2 \cdot sr} \qquad \text{(A-3)}$$

Lastly, we calculate the intensity of the source through the relation $I = LA\cos q_s$ where q_s is the viewing angle made from the source to the detector (see Figure A-1). In this calculation, the angle is assumed to be zero. Thus the intensity is seen to be

$$I = 9.721 * 10^{-4} \frac{W}{cm^2 \cdot sr} \cdot 10{,}000 cm^2 \cdot 1 = 9.721 \frac{W}{sr} \qquad \text{(A-4)}$$

Inserting this into the range equation, the resulting maximum range for detection is

$$r = \sqrt{\frac{D^*}{\sqrt{A_d \Delta f}} \frac{I \times A_{enp}}{SNR}}$$
$$r = \sqrt{\frac{5 * 10^8}{\sqrt{0.01 \cdot 125}} \cdot \frac{9.721 \cdot 4p}{2.5}} \qquad \text{(A-5)}$$
$$r = 147800 cm = 1478.00 m$$

At this distance, the chase vehicle could just make out the target with its infrared camera. With the further assumption that the chase vehicle is already well within this range, the camera should be able to detect the target easily.

Appendix B: Calculation of SIMSAT Moments of Inertia

The moments of inertia of the SIMSAT must be correctly calculated in order for both accurate modeling in the Simulink portion of the experiment, as well as for accurate calculations when designing the controller. With reconfiguration of the SIMSAT between major experiment topics comes the need to recalculate its moments of inertia.

A concise manner in which to perform this calculation has been created in the form of a ControlDesk experiment. The experiment, titled, "MOI_test.cdx" must be initially loaded through the dSPACE ControlDesk software (the reader is assumed to have a basic knowledge of both ControlDesk and Matlab). After the moi_test.ppc file has been loaded to the ds1005 platform aboard SIMSAT, the user need only activate the Animation mode and the experiment begins automatically.

The experiment is designed to actuate one reaction wheel during each run. The reaction wheel, is accelerated to 250 rad/sec, and the resulting spacecraft inertial angles are recorded. The test does need to be reconfigured in order to test all three reaction wheels. Two steps are required to accomplish this: 1) in the Simulink model "MOI_test.mdl" the step input needs to be changed to the appropriate direction, and 2) the corresponding output variable in ControlDesk needs to be linked as the recorded variable.

After the completion of the data gathering, the data must be saved. It is saved by default as a Matlab MAT-file. After data from all directions has been gathered, the Matlab file "moi_test.m" can be used to determine the MOI.

The file must be opened and changed to load the appropriate data files that were saved. A simple name change will accomplish this. The data is manipulated in the following fashion.

A time vector is extracted from one of the data sets (they are all identical). Each data set is then parsed to extract the recorded inertial angular movements in the appropriate direction. The data is then stepped in 5% increments to determine the slope along the entire curve of angular displacement v. time. The maximum slope is used as the slope of record. If desired, the user can take data sets in both a positive and negative direction and average the two slope results.

The results of the slope are then used to solve the equation

$$I_{ii} = (I_{rw|i}\Delta\omega_i)/\Delta\Omega_i$$

where ω_I has been fixed to 250 rad/sec for this experiment, and I_{rw} was established as 0.01955 kg·m^2 during the construction of SIMSAT. If the user wishes to change this value, it can be changed in the Simulink model.

Appendix C. New Equipment Specifications

- Cohu camera 4915-2010/0000
    - Near-IR capabilities (approximately 280-1200 nm spectral sensitivity)
    - Contact Mr. David Lane (858) 277-6700 x393 (www.cohu.com)
- Color Video Camera (wired)
    - Model MC-3300
    - Polaris Industries, Inc. (www.polarisusa.com)
- Lens
    - Comiscar/Pentax 6mm F/1.4 lens (part #C60622)
    - Purchased through Cohu (part #AO-06)
- Lens filter
    - CVI Laser Part # LPF-750-1.00
    - This is a circular, one-inch diameter, long pass filter (750 nm and above)
    - (www.cvilaser.com) (800) 296-9541
- Matrox framegrabber
    - Matrox Meteor II (Standard)
    - MIL-Lite enabling software drivers
    - Purchased through distributor EQS Systems (www.eqssystems.com) (800) 729-8084.
- MATLAB Image Acquisition Toolbox
    - Compatibility with major framegrabber manufacturers, including Matrox

    - Interfaces directly with the MIL-Lite drivers, eliminating the need to program the camera in a separate language
    - The Mathworks, Inc. (www.mathworks.com)
- Video Switcher
    - Two inputs/one output
    - Item #15-1952
    - Radio Shack (www.radioshack.com)
- Wireless video transmitters
    - Radio Shack Part # 150-2572

Appendix D. Matlab Program Code

The following code constitutes the two main Matlab programs used during laboratory testing. The first file, `main.m`, initializes the framegrabber, prepares the video stream, and grabs the intermittent frames for evaluation. For each instance of an image grab, it calls the second file, `write2simsat.m`, which calculates the centroid of the image and writes the centroid pixel values to the ds1005 processor aboard the AutoBox.

Additionally, the code for the two files used to generate the data for the space simulations (`main_leo.m`, `formation_leo.m`) is included at the end of this appendix.

main.m

```
function main
%  ------------------------------------------------------------------------
----
% This function will eventually have the following characteristics:
%   - Take a snapshot of input video at incremental time steps
%   - Send the data to a buffer in ds1005 board resident on the SIMSAT
%       -- it will do this via use of the command
%           mlib('Write',destination,'Data',pic_info)
%% ------------------------------------------------------------------------
-----

%Initialize dSPACE MLIB
% mlib('SelectBoard','ds1005');
%
%  ************************************************************
%  This section checks to see if my Simulink application is running.
%  Currently, I have it named hnpds3, but if I change this, make sure
to
%  change it in the DemoApplName line below.
%  ************************************************************

% ************************************************************
%   Image Acquisition Toolbox Portion
%       - this section will take the snapshots and save them to
%       the local hard disk (and memory).
%
```

```
% NOTES:  If memory is getting too full and I have to remove frames,
this is
% done with the 'getdata' of 'flushdata' commands.  See page 4-22, -30.
% If I want to increase the memory capacity, see page 4-29.
%
%   I can create a memory monitoring function by example on page 6-16.
%
% ************************************************************
n = 1;      % Actually the value of FramesPerTrigger
hwinfo = imaqhwinfo;
vid = videoinput('matrox');
preview(vid)
pause
closepreview(vid)
vid.LoggingMode = 'memory';
vid.FramesPerTrigger = n;
vid.FrameGrabInterval = 330;
vid.FramesAcquiredFcn = @write2simsat;
vid.FramesAcquiredFcnCount = 1;
vid.TriggerFrameDelay = 90;    % wait 3 seconds after I hit the trigger
triggerconfig(vid,'manual');
start(vid)
disp('video started')

% ************************************************************
%   Initiate Trigger (start the acquisition of desired number of
frames).
%   Prior to this point, the video stream has started, but it is not
%   logging the specific frames that I want.  I will issue the pause
%   command, and then, when I am ready (and ControlDesk is ready) to
%   proceed, just hit any key in the Matlab workspace.  The function
will
%   begin running again, and the first command it encounters will be
the
%   trigger to get things going.
% ************************************************************

pause
trigger(vid)

%   WORKING ITS MAGIC HERE -- calls to other m-files

%if(exist(IRpics)==2)
%    disp('AVI file created.')
%end
%aviobj = close(vid.DiskLogger);
%vid.FramesAcquired     % This is called in @write2simsat
wait(vid);
stop(vid);
disp('video stopped')
%vid.FramesAcquired
frames = getdata(vid,n);
imaqmontage(frames);
delete(vid);
clear vid
```

write2simsat.m

```
function write2simsat(vid,FramesAcquiredFcn)

type = 'unit8';             % I think this is correct, may have to
change (or remove altogether)
newest_pic = getdata(vid,1);
imaqmontage(newest_pic)     % I can do away with this line if I want
to.
%framesacquired = vid.FramesAcquired
%frameswritten  = vid.DiskLoggerFrameCount

% Get descriptors for the state space matrices
matrix = {'Model Root/Spring-Mass-Damper System/Spring-Mass-Damper
System/A'};

[IR_pic_matrix_desc] = mlib('GetTrcVar',matrix);
%[Amatrix_desc, Cmatrix_desc] = mlib('GetTrcVar',matrices);

mlib('Write',IR_pic_matrix_desc,'Data', newest_pic);
sprintf ('Image Written to ds1005.\n');

% Input times when parameters are updated
update_time = input(' Update interval               [1 sec]  ?  ');
if isempty(update_time), update_time=1; end;
fprintf (' ------------------------------------------\n');

% Start MATLAB stopwatch timer (min. timer resolution 54 ms)
tic; T=0;
for damp=damp_values,
  % Compute transfer function parameters of spring-mass-damper system
  amatrix = [ -2*damp*OMEGA -OMEGA*OMEGA ];   % [ -a1 -a0 ]

  % Write new transfer function parameters to real-time processor
  mlib('Write',Amatrix_desc,'Data', amatrix);
  fprintf ('T=%5.2f sec. Damping factor is now %5.2f,...\n', T, damp);

  % Let background processes become active while waiting
  T = T + update_time;
  while (toc < T), end;
end
fprintf (' ------------------------------------------\n');
```

main_leo.m

```
%*******************************************
%
%
%    ****************************************
%    ****************************************
%
%   This program is designed to calculate the INITIAL position and
```

```
%   velocity vectors of a reference orbit as well as a second orbit
%   situated nearby.  The code is broken into three parts.  The
%   objective of each part is discussed in its header.
%
%   Several outside programs were provided in order to propagate the
%   orbit(s) forward and visualize them.  These are not called from
%   this program, rather, the outputs of this program are entered into
%   the file formation.m (courtesy Dr. Steven Tragesser, AFIT.)
%
%       Accompanying notes scattered throughout the project should
%       alleviate any confusion on parameters.
%
%*********************************************

%*********************************************
%
%  PART I
%
%  In this section, a reference orbit is defined.  The reference orbit
%  is output in the J2000 frame with IJK coordinates.  The launch time
%  and initial reference orbital elements are obtained (a,e,i,Om,u).
%  Lastly, the orbit is plotted for thirty days after the launch using
%  the file 'orbitJ2.m.'
%
%*********************************************
global mu
disp(blanks(1)')
r = 7000;                       % km, given
a = 7000;                       % km, given
e = 0;                          % given
lat = 34.7;                     % deg, given
lat_rad = 34.7*pi/180;
Om_dot = (360/365.25)*pi/180;   % rad/day, Tropical Year assumed
Om_dot = Om_dot/86400;          % rad/sec
r_earth = 6378.145;             % km
J2 = 0.001082;                  % obtained from BMW
n = sqrt(398601/(7000^3));      % rad/sec
cosi = (-1)*(Om_dot*2*(a^2)*((1 - e^2)^2))/(3*n*J2*(r_earth^2));
i_rad = acos(cosi);
i = i_rad*180/pi;               % deg
Az_rad = asin((cos(i_rad)/cos(lat_rad)));
Az = Az_rad*180/pi;
Az = 180 + abs(Az);     % NOTE: This equation is not universally valid;
it is specific to a retrograde orbit, launching into descending node.

n_earth = (360/365.25)*pi/180;       % rad/day, Earth's mean motion
about the sun
days = 25 + (1/24);
mean_sun_angle = n_earth*days*180/pi;
more_deg = 0;
more_time = 1.5;
old_launch_time = 0;
while more_time > 1
    Om = 360-mean_sun_angle-30 - more_deg;
    delta_rad = asin(tan(lat_rad)*cot(i_rad));
```

```
    delta = delta_rad*180/pi;
    w_earth = 360/86164;
    alpha_g = (36831/86164)*360;
    lambda_e = 360-120.5;
    to = 0;
    launch_time = to + (Om + 180 - delta - alpha_g - lambda_e)/w_earth;
    more_deg = (launch_time-old_launch_time)*n_earth*180/pi/86400;
    more_time = more_deg/w_earth;
    old_launch_time = launch_time;
end
Om;
launch_time = sec2hr(launch_time);
launch_time = hr2hms(launch_time);
launch_time = hms2mat(launch_time);

%   Finding u -- argument of latitude; taken from spherical trig
Lecture Notes 10.3

theta = Az - 180;
theta_rad = theta*pi/180;
i1 = 180-i;
i1_rad = i1*pi/180;
i2 = 90;    %cos i2 = 0
u1 = acos((cos(i1_rad)*cos(theta_rad))/(sin(i1_rad)*sin(theta_rad)));
u1 = u1*180/pi;
u = 180- u1;
elements = [a; e; i; Om; u;]

% Find r and v vectors in J2000 frame

mu = 398601;    % km^3/sec^2
nu1 = u*pi/180;
format long g
p = (a*(1 - e^2));
r_pqw = (a*(1 - e^2))/(1 + e*cos(nu1));
r_sat_pqw = [cos(nu1); sin(nu1); 0]*r_pqw;
v_pqw = sqrt(mu/p);
v_sat_pqw = v_pqw*[-sin(nu1); (e + cos(nu1)); 0];

%************************************************
% Now the PQW vector must be rotated to the ECI (or J2000) frane.
w = 0;
format long g
Om_rad = (Om*pi)/180;
w_rad = (w*pi)/180;
R = [(cos(Om_rad)*cos(w_rad) - sin(Om_rad)*sin(w_rad)*cos(i_rad)) (-
cos(Om_rad)*sin(w_rad) - sin(Om_rad)*cos(w_rad)*cos(i_rad))
(sin(Om_rad)*sin(i_rad)); (sin(Om_rad)*cos(w_rad) +
cos(Om_rad)*sin(w_rad)*cos(i_rad)) (-sin(Om_rad)*sin(w_rad) +
cos(Om_rad)*cos(w_rad)*cos(i_rad)) (-cos(Om_rad)*sin(i_rad));
(sin(w_rad)*sin(i_rad)) (cos(w_rad)*sin(i_rad)) cos(i_rad)];
r_ref_J2000 = R*r_sat_pqw     %previously known as r_sat_eci
v_ref_J2000 = R*v_sat_pqw     %previously known as v_sat_eci

%*********************************************************
```

```
%   PART II
%
%   We now seek to find the position and velocity vectors of the three
%   satellites with respect to an XYZ orbit which moves relative to
%   IJK.
%
%   The equations used here are derived from the constraints required
%   for a centered in-plane ellipse.  The constraints are taken from
%   Lovell & Tragesser, Paper AAS 03-139.
%
%       For the chief to be centered, yo = (2/n)*xo_dot
%
%*********************************************************

% Sat 1
xo = 0;         % kilometers
yo = .100;
zo = 0;         % km

xd = 0;yd = 0;
yr = -1.5*n*xd;
beta = pi/2; %corresponds to starting at right edge of ellipse
xo_dot = yo*n/2;
yo_dot = (xd - (4*xo))*n/2;
zo_dot = 0;

Sat1_Pos_XYZ = [xo;yo;zo]

Sat1_Vel_XYZ = [xo_dot;yo_dot;zo_dot]

%*********************************************************
%   PART III
%
%   We now rotate the XYZ frame to the IJK frame to obtain the
%   position and velocity vectors for each of the three satellites in
%   the IJK frame.  Afterwards, the results will be input to propagate
%   forward for ten hours to see the interactions of the satellites
%   while on orbit.
%
%*********************************************************

u_rad = u*pi/180;
Rxyz2ijk = [(cos(Om_rad)*cos(u_rad) -
sin(Om_rad)*sin(u_rad)*cos(i_rad)) (-cos(Om_rad)*sin(u_rad) -
sin(Om_rad)*cos(u_rad)*cos(i_rad)) (sin(Om_rad)*sin(i_rad));
    (sin(Om_rad)*cos(u_rad) + cos(Om_rad)*sin(u_rad)*cos(i_rad)) (-
sin(Om_rad)*sin(u_rad) + cos(Om_rad)*cos(u_rad)*cos(i_rad)) (-
cos(Om_rad)*sin(i_rad));
    (sin(u_rad)*sin(i_rad)) (cos(u_rad)*sin(i_rad)) cos(i_rad)];

Sat1_Pos_J2000 = Rxyz2ijk*Sat1_Pos_XYZ;

Sat1_I_Pos_Final = Sat1_Pos_J2000(1,1) + r_ref_J2000(1,1);
Sat1_J_Pos_Final = Sat1_Pos_J2000(2,1) + r_ref_J2000(2,1);
Sat1_K_Pos_Final = Sat1_Pos_J2000(3,1) + r_ref_J2000(3,1);
```

```
Sat1_Final_Pos = [Sat1_I_Pos_Final;Sat1_J_Pos_Final;Sat1_K_Pos_Final]

%****************************************
%% Find velocity vectors
%****************************************

Om_dot = 0; %This is due to the fact that the Clohessey-Wiltshire eq.s
were not developed with the J2 parameter taken into account.  So we set
it equal to zero in this matrix.
R_dot_xyz2ijk = [(Om_dot*cos(u_rad)*(-sin(Om_rad)) + cos(Om_rad)*(-
sin(u_rad))*n - cos(Om_rad)*sin(u_rad)*cos(i_rad)*Om_dot -
cos(i_rad)*cos(u_rad)*sin(Om_rad)*n), (sin(Om_rad)*sin(u_rad)*Om_dot -
cos(Om_rad)*cos(u_rad)*n - cos(Om_rad)*cos(u_rad)*cos(i_rad)*Om_dot +
sin(u_rad)*sin(Om_rad)*cos(i_rad)*n) , (cos(Om_rad)*sin(i_rad)*Om_dot)
;
    (cos(Om_rad)*cos(u_rad)*Om_dot - sin(u_rad)*sin(Om_rad)*n -
sin(Om_rad)*sin(u_rad)*cos(i_rad)*Om_dot +
cos(u_rad)*cos(Om_rad)*cos(i_rad)*n), (-cos(Om_rad)*sin(u_rad)*Om_dot -
sin(Om_rad)*cos(u_rad)*n - sin(Om_rad)*cos(u_rad)*cos(i_rad)*Om_dot -
sin(u_rad)*cos(Om_rad)*cos(i_rad)*n), (sin(Om_rad)*sin(i_rad)*Om_dot);
    (cos(u_rad)*sin(i_rad)*n), (-sin(u_rad)*sin(i_rad)*n), 0];

Sat1_Final_Vel = v_ref_J2000 + R_dot_xyz2ijk*Sat1_Pos_XYZ +
Rxyz2ijk*Sat1_Vel_XYZ
[next,tspan,zref,norm_vec] =
formation_leo(r_ref_J2000,v_ref_J2000,Sat1_Final_Pos,Sat1_Final_Vel);
```

formation_leo.m

NOTE: Credit is given to Dr. Steven Tragesser (AFIT) for the foundation of this code.

```
function [next,tspan,zref,norm_vec] =
formation_leo(r_ref,v_ref,r_ref1,v_ref1)

global mu

%%%%%%%%%%%%%%%%%%%%%%%%%%%%%%%%%%%%%%%%%%%%%%%%%%%%%%%%%%%%
%  Inputs: r and v in J2000 coordinates (km and km/s)
%%%%%%%%%%%%%%%%%%%%%%%%%%%%%%%%%%%%%%%%%%%%%%%%%%%%%%%%%%%%

sim_time=12*3600;    %in seconds
J2_flag=1;           %0=spherical Earth   1=oblate Earth

Simulation parameters
Tspan = [0:sim_time/200:sim_time];
if J2_flag==0
    eoms = 'twobodyeoms3d';
else
    eoms = 'twobodyeoms3dj2';
end

%%%%%%%%%%%%%%%%%%%%%%%%%%%%%%%%%%%%%%%%%%%%%%%%%%%%%%%%%%%%
```

```
% Set up and plot reference orbit

z0=[r_ref' v_ref'];
options=odeset('RelTol',1e-10,'AbsTol',1e-8*ones(6,1));
options2 = odeset('RelTol',1e-10,'AbsTol',1e-8);
[tref,zref]=ode45(eoms,tspan,z0,options);
zref;



        r_ref=r_ref1;
        v_ref=v_ref1;
        symbol='r.';

% Simulation of EOMS of deputy
% Set initial condition of deputy
z0=[r_ref' v_ref'];
% Call integrator
options=odeset('RelTol',1e-10,'AbsTol',1e-8*ones(6,1));
[tref,z]=ode45(eoms,tspan,z0,options);
[tref2,theta] = ode45(@ode_leo_thetadot,tspan,0,options2);
num_pts=size(tspan,2);
% Set up box
    rhat=zref(1,1:3)'/norm(zref(1,1:3));
    vhat=zref(1,4:6)';
    hhat=cross(rhat,vhat)/norm(cross(rhat,vhat));
    thhat=cross(hhat,rhat)/norm(cross(hhat,rhat));
    Ri2o=[rhat'; thhat'; hhat'];
    rorb(1,1:3)=(Ri2o*z(1,1:3)')';
    rmag(1)=norm(zref(1,1:3));
    r = rorb(1,1)-rmag';
    s = rorb(1,2);
    w = rorb(1,3);
    a = [(r-.005) (s-.005) (w-.005); (r+.005) (s-.005) (w-.005);
(r+.005) (s+.005) (w-.005);...
        (r-.005) (s+.005) (w-.005); (r-.005) (s-.005) (w+.005);
(r+.005) (s-.005) (w+.005);...
        (r+.005) (s+.005) (w+.005); (r-.005) (s+.005) (w+.005)];
    b = [1 2 6 5; 2 3 7 6; 3 4 8 7; 4 1 5 8; 1 2 3 4; 5 6 7 8];
    %box =
patch('Vertices',a,'Faces',b,'FaceVertexCData',hsv(6),'FaceColor','flat
');
    theta_last = 0;%axis([-.2 .2 -.2 .2 -.2 .2]); axis square;break

% Motion
for ii=1:num_pts
   %transform position from inertial to orbit frame
   rhat=zref(ii,1:3)'/norm(zref(ii,1:3));
   vhat=zref(ii,4:6)';
   hhat=cross(rhat,vhat)/norm(cross(rhat,vhat));
   thhat=cross(hhat,rhat)/norm(cross(hhat,rhat));
   Ri2o=[rhat'; thhat'; hhat'];     % transforms from inertial to RSW
frame
   rorb(ii,1:3)=(Ri2o*z(ii,1:3)')';
   rchief(ii,1:3) = (Ri2o*zref(ii,1:3)')';
```

```
   rmag(ii)=norm(zref(ii,1:3));
   r = rorb(:,1)-rmag';
   s = rorb(:,2);
   w = rorb(:,3);
   r_now(ii) = rorb(ii,1)-rmag(ii);
   s_now(ii) = rorb(ii,2);
   w_now(ii) = rorb(ii,3);
   r_chief_now(ii) = rchief(ii,1)-rmag(ii);
   s_chief_now(ii) = rchief(ii,2);
   w_chief_now(ii) = rchief(ii,3);
   line(r,s,w);hold on
   plot3(r_chief_now,s_chief_now,w_chief_now,'r.');
   %new_vertices = [(r_now(ii)-.005) (s_now(ii)-.005) (w_now(ii)-.005);
(r_now(ii)+.005) (s_now(ii)-.005) (w_now(ii)-.005); (r_now(ii)+.005)
(s_now(ii)+.005) (w_now(ii)-.005);...
        %(r_now(ii)-.005) (s_now(ii)+.005) (w_now(ii)-.005);
(r_now(ii)-.005) (s_now(ii)-.005) (w_now(ii)+.005); (r_now(ii)+.005)
(s_now(ii)-.005) (w_now(ii)+.005);...
        %(r_now(ii)+.005) (s_now(ii)+.005) (w_now(ii)+.005);
(r_now(ii)-.005) (s_now(ii)+.005) (w_now(ii)+.005)];
   %set(box,'Vertices',new_vertices,'Faces',b);
   theta_inc = theta(ii) - theta_last;
   theta_deg_inc = theta_inc*180/pi;
   %origin = [r_now(ii) s_now(ii) w_now(ii)];
   %rotate(box,[0 0 1],(-180/pi)*theta(ii),origin);
   %axis([-.2 .2 -.2 .2 -.2 .2]); axis square;
   %M(ii) = getframe;
   offset(ii,1) = (r_now(ii) - r_chief_now(ii));
   offset(ii,2) = (s_now(ii) - s_chief_now(ii));
   offset(ii,3) = (w_now(ii) - w_chief_now(ii));
   norm_vec(ii) = sqrt((offset(ii,1)^2) + (offset(ii,2)^2) +
(offset(ii,3)^2));
   phi(ii) = atan2(offset(ii,1),offset(ii,2));      %phi is "true"
angular offset
   theta_last = theta(ii);
end

xlabel('x (km)')
ylabel('y (km)')
zlabel('z (km)')
if J2_flag == 0
    title('Deputy Motion in Orbital Reference Frame -- Unperturbed')
else
    title('Deputy Motion in Orbital Reference Frame -- J2 Perturbed')
end

next = [(-1)*((phi')),(-1)*(mod(theta,(2*pi)))];
```

Appendix E. Characterization of Yaw Gyro Drift

Gyro drift has previously been identified as a problem encountered with SIMSAT. Though the pitch gyro is the most sensitive, all three gyros are subject to the drift phenomenon. A study of the drift for the yaw gyro was undertaken to better characterize it for the purposes of this study.

Previous users had claimed an improvement in gyro performance after a long period of warm-up time. Thus, the gyro drift was investigated after different amounts of usage. The SIMSAT was fixed in its stand so that no actual movement could take place. Whatever movement then reported back by the gyros was obviously in error.

Figure E-1 shows the gyro drift rates taken after increasing amounts of warm-up time. 10-minute samples were taken immediately after gyro turn-on ("zero" minutes), after 20 minutes of usage, 50 minutes of usage, and 60 minutes of usage. Under normal circumstances, the batteries will not last much longer than an hour, so the tests were halted at this point.

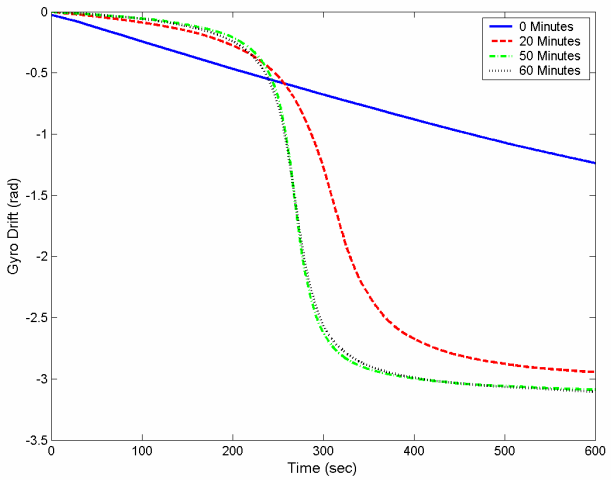

Figure E-1. Yaw Gyro Drift Angles after Various Amounts of Warm-up Time

As is evident, there is a distinct difference in the behavior of the gyro as it is allowed to warm up. Immediately upon start-up, the yaw gyro exhibits a linear decay in reported angle. As time goes on, it appears to come to a limit; the 50 minute and 60 minute plots lie almost on top of one another.

For the purposes of this paper, the four results were averaged over only the first 200 seconds of reported data. A second order polynomial was fit to this data. This polynomial was then used in the satellite model to offset the reported orientation angle. Figure E-2 shows the averaged gyro drift four all four cases over the fist 200-second interval, as well as the second-order polynomial fit line.

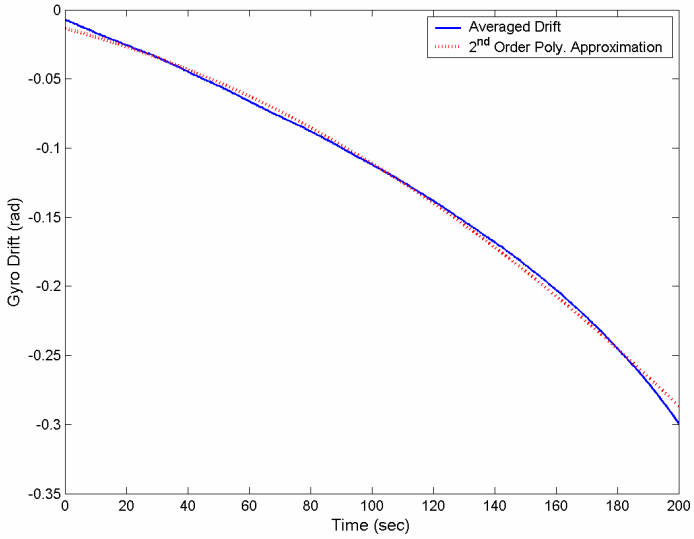

Figure E-2. Average Yaw Gyro Drift and a Polynomial Approximation

Appendix F. Simulation Model Library

The following Simulink diagrams represent those used in the testing of the laboratory experiment. Figures F1 through F6 are those used in the software modeling of the laboratory equipment. Figures F7 through F10 are those used in the actual hardware-in-the-loop experiments.

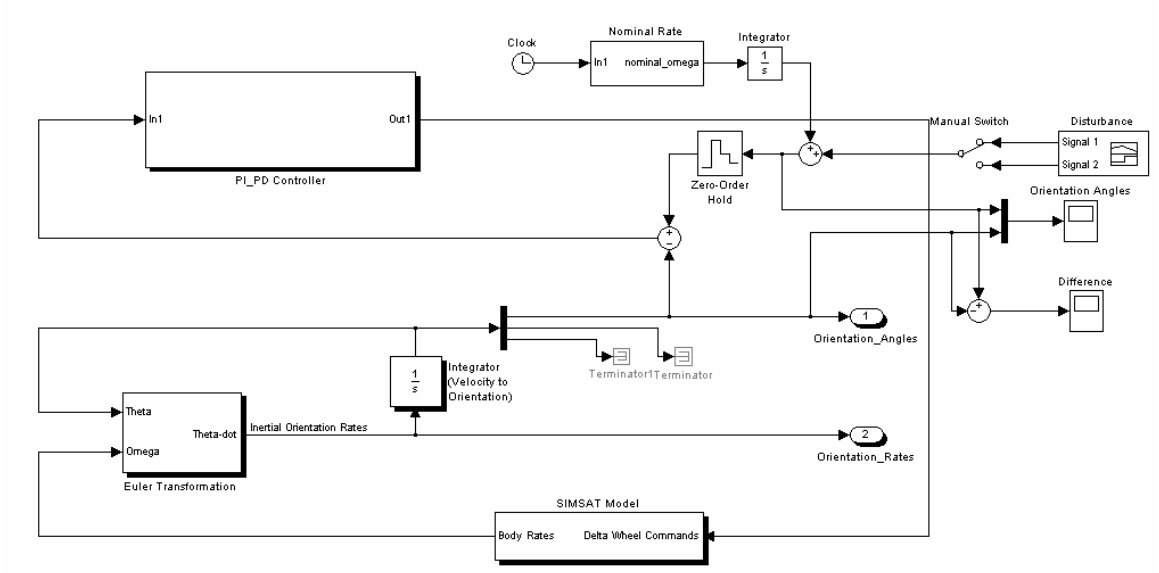

Figure F1. Top-Level System Diagram of Software Model

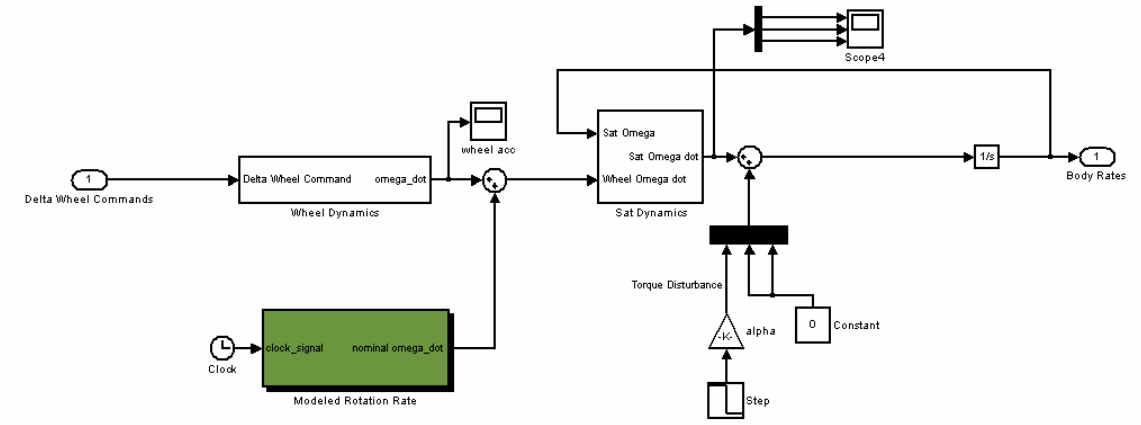

Figure F2. SIMSAT Model Sublevel Diagram

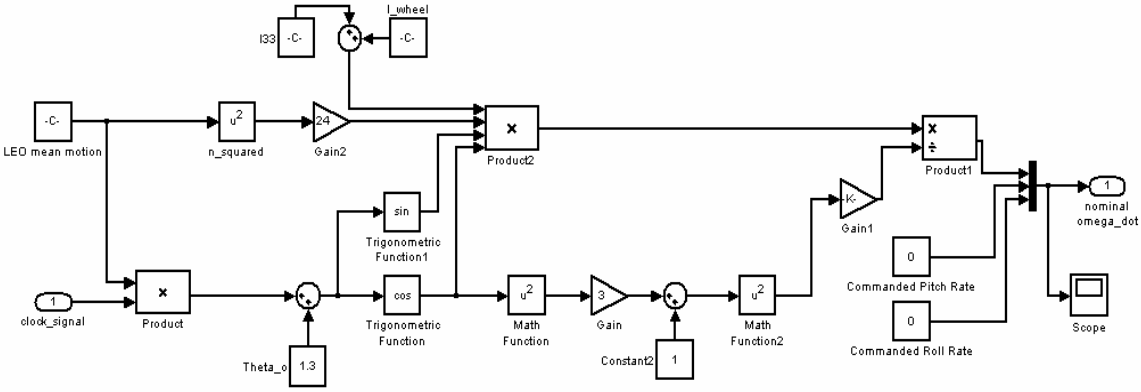

Figure F3. Modeled Rotation Rate Sub-sublevel Diagram

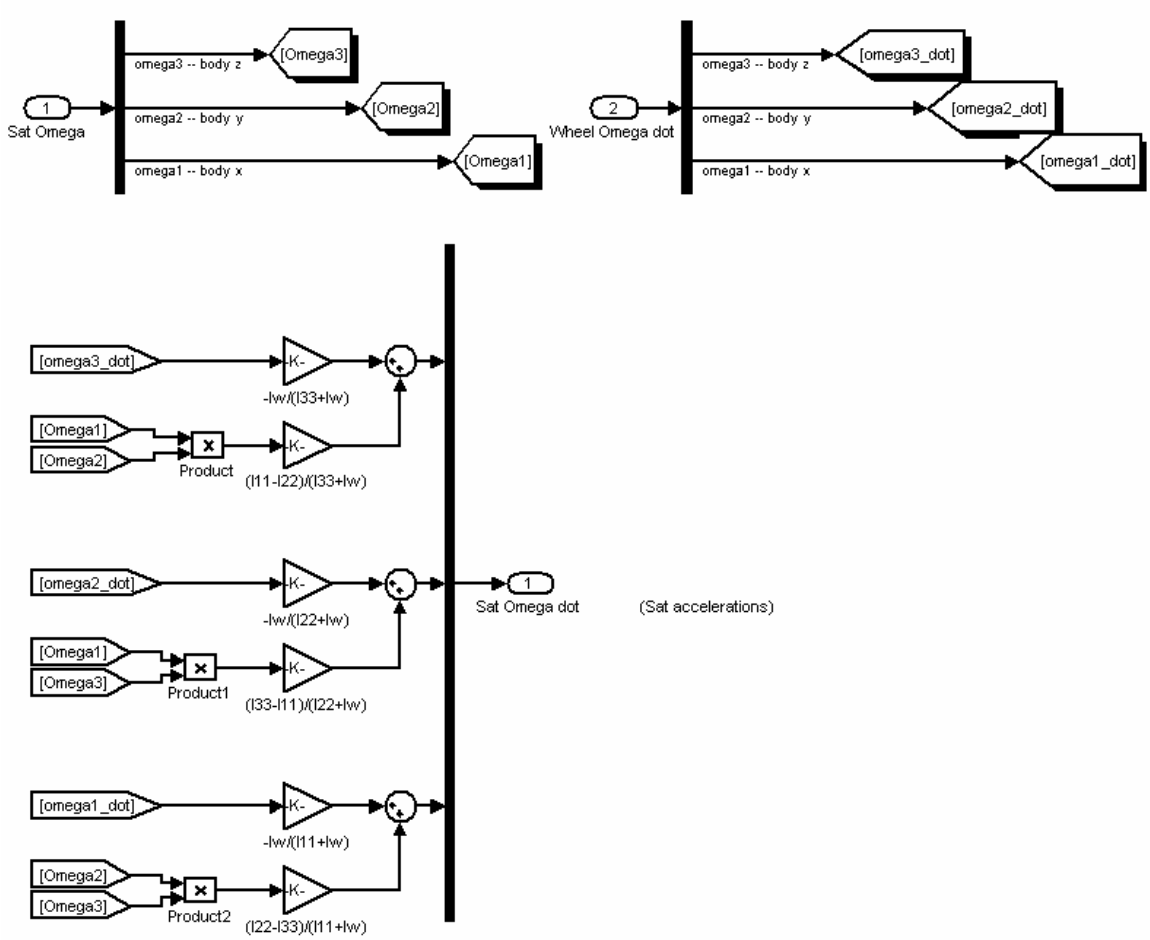

Figure F4. Sat Dynamics Sub-sublevel Diagram

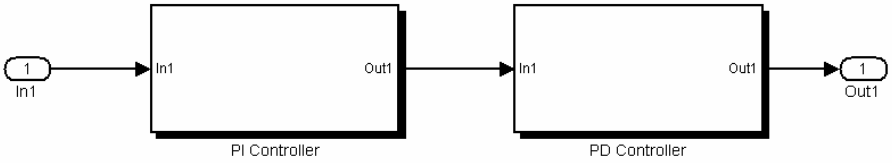

Figure F5. PI_PD Controller Sublevel Diagram

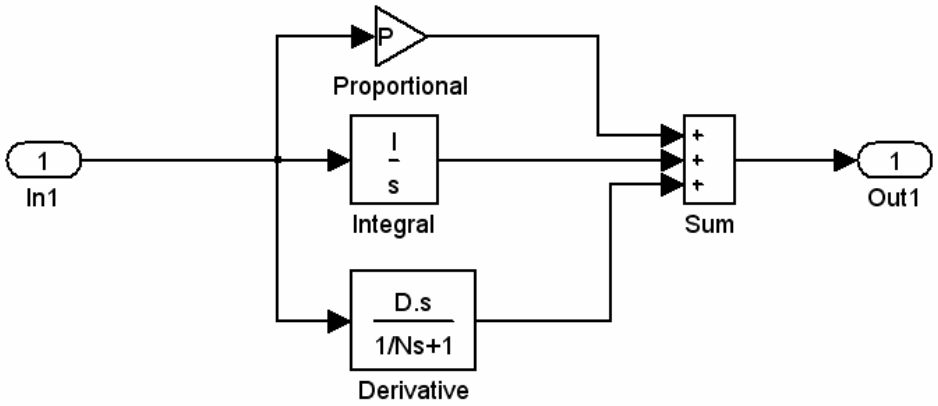

Figure F6. PI_(PD_)Controller Sub-sublevel Diagram

Figure F8. System-level Diagram of Software Model

Figure F9. System-level Diagram of Software Model

Figure F10. System-level Diagram of Software Model

Figure F11. System-level Diagram of Software Model

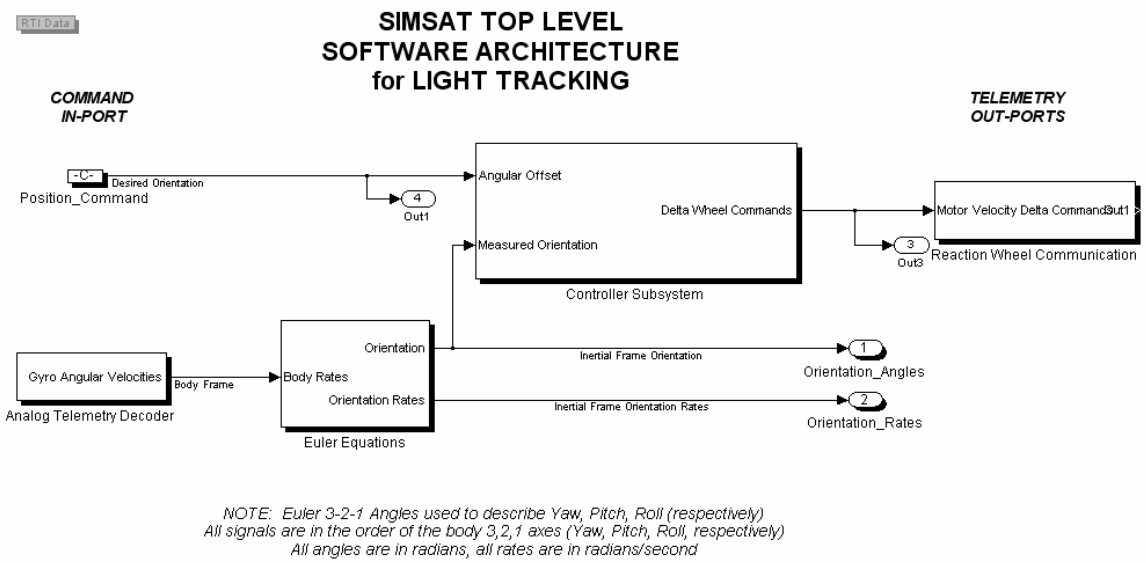

Figure F7. System-level Diagram of Software Model

Bibliography

1. Amptek Inc. "CEASE: Space Radiation Alarm." Company brochure. n. pag. http://www.amptek.com/pdf/cease.pdf.

2. Banke, Jim. "Air Force XSS-10 Micro-Satellite Mission a Success." http://dev.space.com/missionlaunches/xss10_update_030130.html.

3. Canan, James A. "Controlling the Space Arena," *Aerospace America*, vol: pp-pp (January 2004).

4. Capper, Peter and C.T. Elliott, et al. *Infrared Detectors and Emitters: Materials and Devices*. Norwell Massachusetts: Kluwer Academic Publishers, 2001.

5. Chobotov, Vladimir A. *Orbital Mechanics*. City: American Institute of Aeronautics and Astronautics, 2002.

6. Department of the Air Force. *Space Handbook: A War Fighter's Guide to Space.* Air University Publication 18. Air University Press, Maxwell AFB AL: 1993.

7. Dereniak, E.L., and G.D. Boreman. *Infrared Detectors and Systems.* USA: Wiley-Interscience, 1996.

8. Doebelin, Ernest O. *Measurement Systems: Application and Design*. North Bergen New Jersey: Book-Mart Press, 1990.

9. Elachi, Charles. *Introduction to the Physics and Techniques of Remote Sensing*. USA: Wiley-Interscience, 1987.

10. Foust, Jeff. "Spied Satellites." Excerpt from unpublished article. n. pag. http://thespacereview.com/article/46/1. 9 September 2003.

11. Gilmore, David G. and others. *Spacecraft Thermal Control Handbook*. El Segundo California: The Aerospace Press, 2002.

12. Ginsberg, Jerry H. *Advanced Engineering Dynamics.* New York: Cambridge University Press, 1998.

13. Indigo Systems. "Omega Specifications." Company brochure. n. pag. http://www.inidgosystems.com

14. Irvin, David J., Jr. *A Study of Linear vs. Non-Linear Control Techniques for the Reconfiguration of Satellite Formations*. MS Thesis, AFIT/GA/ENY/01M-02. School of Engineering and Management, Air Force Institute of Technology (AU), Wright-Patterson AFB OH, March 2002.

15. Junkins, John L., and others. "Vision-based Navigation for Rendezvous, Docking, and Proximity Operations." *Proceedings of the IEEE International Conference on Robots & Automation, 2000*. Paper AAS 99-021.

16. Koryakin, A.V. "Structural-Topological Model of Spacecraft Images Formed Using a Photodetector Array under Different Monitoring Conditions of Observation." *Pattern Recognition and Image Analysis.* Vol. 11, No. 1, 2001, pp 202-204.

17. Lovell, T.A., and S.G. Tragesser. "Analysis of the Reconfiguration and Maintenance of Close Spacecraft Formations," *13th AAS.AIAA Space Flight Mechanics Meeting*. Paper AAS 03-139.

18. Mitsushige, Oda. "Experiences and Lessons Learned from the ETS-VII Robot Satellite," *Proceedings of the IEEE International Conference on Robots & Automation, 2000*. 914-919. New York: IEEE Press, 2000.

19. National Security Space Architect. "NSSA Space Situational Awareness Architecture." Excerpt from conference notes. http://www.spacecoretech.org/coretech2002/Papers/Space%20Situation%20Awareness/pdfs/NSSA%20Briefing%20to%20Core%20Technologies%20Conference.pdf19 November 2002.

20. Ogata, Katsuhiko. *Modern Control Engineering*. Upper Saddle River New Jersey: Prentice Hall, 2002.

21. Rees, W.G. *Physical Principles of Remote Sensing*. New York: Cambridge University Press, 2001.

22. Reilly, J. Patrick, and others. "Design and Demonstration of an Infrared Passive Ranger." *Johns Hopkins APL Technical Digest*. Volume 20, No. 2, 1999. pp. 220-235.

23. Sietzen, Frank, Jr. "Microspace Technology Comes to China." Excerpt from unpublished article. n. pag. http://www.space.com/news/spaceagencies/microsat_china_001019.html. 19 October 2000.

24. *Space Object Identification*. Contract N00014-97-D-2014/001, Albuquerque NM: Schafer Corporation, February 1999.

25. Tragesser, Steven G. Class handout, MECH 533, Intermediate Spaceflight Dynamics. School of Engineering and Management, Air Force Institute of Technology, Wright-Patterson AFB OH, April, 2003.

26. Tschirhart, Troy A. *A Study of Control Laws for Microsatellite Rendezvous with a Noncooperative Target*. MS Thesis, AFIT/GAI/ENY/03-3. School of Engineering and Management, Air Force Institute of Technology (AU), Wright-Patterson AFB OH, March 2003.

27. Whelan, David A. and others. "The DARPA Orbital Express Program: Effecting a Revolution in Space-Based Systems," *Proceedings of SPI.* 48-56. New York: SPIE, 2001.

28. Wiesel, William. *Spaceflight Dynamics*. USA: McGraw-Hill, 1997.

29. Wilson, Tom. *Threats to United States Space Capabilities.* Prepared for the Commission to Assess United States National Security Space Management and Organization. Washington: GPO, 2001.

30. Worden, Simon P. "New Directions for National Security Space Programs," *Space Access and Utilization Beyond 2000; Proceedings of the Symposium*. 133-43. San Diego CA: Univelt, Inc. 2001.

31. www.heavens-above.com. Providers of astronomical data. http://www.heavens-above.com/orbitdisplay.asp?Session=kebgcfldhndnhkfgfidclpid&satid=5588.

Vita

Capt Matt Kimsal graduated from Michigan State University in 1998 with a BS in Mechanical Engineering. He entered the Air Force in February of 1999 and was first stationed at Vandenberg AFB, CA, where he was a student at the 392d Training Squadron in Undergraduate Space and Missile Training. He was subsequently assigned to the 4th Space Operations Squadron at Schriever AFB, CO as a Satellite Vehicle Operator for the Milstar program. While at Schriever, he was reassigned as an evaluator for the 50th Operations Group. Following AFIT, Capt Kimsal will be assigned to the Space Vehicles Directorate of the Air Force Research Laboratory at Kirtland AFB, NM.

REPORT DOCUMENTATION PAGE

Form Approved
OMB No. 074-0188

1. REPORT DATE *(DD-MM-YYYY)*	**2. REPORT TYPE**	**3. DATES COVERED** *(From – To)*
23 Mar 04	**Master's Thesis**	18 Aug 02 – 23 Mar 04

4. TITLE AND SUBTITLE

DESIGN OF A SPACE-BORNE AUTONOMOUS INFRARED TRACKING SYSTEM

5a. CONTRACT NUMBER

5b. GRANT NUMBER

5c. PROGRAM ELEMENT NUMBER

6. AUTHOR(S)

Kimsal, Matthew, B., Captain, USAF

5d. PROJECT NUMBER
If funded, enter ENR #

5e. TASK NUMBER

5f. WORK UNIT NUMBER

7. PERFORMING ORGANIZATION NAMES(S) AND ADDRESS(S)
Air Force Institute of Technology
Graduate School of Engineering and Management (AFIT/EN)
2950 Hobson Way
WPAFB OH 45433-7765

8. PERFORMING ORGANIZATION REPORT NUMBER

AFIT/GA/ENY/04-M02

9. SPONSORING/MONITORING AGENCY NAME(S) AND ADDRESS(ES)
Withheld

10. SPONSOR/MONITOR'S ACRONYM(S)

11. SPONSOR/MONITOR'S REPORT NUMBER(S)

12. DISTRIBUTION/AVAILABILITY STATEMENT
APPROVED FOR PUBLIC RELEASE; DISTRIBUTION UNLIMITED.

13. SUPPLEMENTARY NOTES

14. ABSTRACT

Complete characterization of the Space environment in support of the United States' goal of Space Situational Awareness is not currently achievable. When confronted with recent increases in the deployment and miniaturization of microsatellites by numerous nations, the questions of foreign Space capabilities are magnified. This study sought to determine the feasibility of and experimentally demonstrate a microsatellite capability to autonomously loiter about and track a target satellite.

Various methods of passive remote sensing were investigated to determine the best means of detecting and tracking a target in space. Microbolometer-based infrared sensors were identified as the best alternative. A representative system was constructed for demonstration in AFIT's SIMSAT laboratory.

Software modeling results identified open-loop instability, and therefore the requirement for closed-loop control. A simple PD control algorithm served as the basis for control, and a pseudo-feed-forward term was added to improve results. The feed-forward term was derived form orbital dynamics as the rate at which the chase satellite traverses around an ellipse formed in the target's frame of reference. Reduction in pointing errors of up to 67% were found in simulations. Non-optimal yet successful tracking results were obtained in the laboratory with a hardware-in-the-loop model for both step and moving inputs.

15. SUBJECT TERMS
Infrared radiation, Non-cooperative, Autonomous, Passive systems, Microsatellite, Rendezvous spacecraft, Satellite Tracking Systems

16. SECURITY CLASSIFICATION OF:			**17. LIMITATION OF ABSTRACT**	**18. NUMBER OF PAGES**	**19a. NAME OF RESPONSIBLE PERSON**
REPORT	**ABSTRACT**	**c. THIS PAGE**			Maj Richard Cobb
U	**U**	**U**	**UU**	101	**19b. TELEPHONE NUMBER** *(Include area code)* (937) 255-6565, ext 4559; e-mail: richard.cobb@afit.edu